1 **Asymmetrical localization of Nup107-160 subcomplex components within the**

2 **nuclear pore complex in fission yeast**

3

4 *Haruhiko Asakawa[1], Tomoko Kojidani[2,3], Hui-Ju Yang[1], Chizuru Ohtsuki[1], Hiroko

5 Osakada[2], Atsushi Matsuda[2], Masaaki Iwamoto[2], Yuji Chikashige[2], Koji Nagao[4,5],

6 Chikashi Obuse[4,5], *Yasushi Hiraoka[1,2] & *Tokuko Haraguchi[1,2]

7

8 [1] Graduate School of Frontier Biosciences, Osaka University, Suita, Japan

9 [2] Advanced ICT Research Institute Kobe, National Institute of Information and

10 Communications Technology, Kobe, Japan

11 [3] Department of Chemical and Biological Sciences, Faculty of Science, Japan Women's

12 University, Tokyo, Japan

13 [4] Graduate School of Life Science, Hokkaido University, Sapporo, Japan.

14 [5] Graduate School of Science, Osaka University, Toyonaka, Japan.

15

16 *Corresponding authors:

17 Tokuko Haraguchi

18 e-mail: tokuko@nict.go.jp

19 Yasushi Hiraoka

20 e-mail: hiraoka@fbs.osaka-u.ac.jp

21 Haruhiko Asakawa

22 e-mail: askw@fbs.osaka-u.ac.jp

23

Abstract

24

25 The nuclear pore complex (NPC) forms a gateway for nucleocytoplasmic transport. The

26 outer ring protein complex of the NPC (the Nup107-160 subcomplex in humans) is a

27 key component for building the NPC. Nup107-160 subcomplexes are believed to be

28 symmetrically localized on the nuclear and cytoplasmic sides of the NPC. However, in

29 *S. pombe* immunoelectron and fluorescence microscopic analyses revealed that the

30 homologous components of the human Nup107-160 subcomplex had an asymmetrical

31 localization: constituent proteins spNup132 and spNup107 were present only on the

32 nuclear side (designated the spNup132 subcomplex), while spNup131, spNup120,

33 spNup85, spNup96, spNup37, spEly5 and spSeh1 were localized only on the

34 cytoplasmic side (designated the spNup120 subcomplex), suggesting the complex was

35 split into two pieces at the interface between spNup96 and spNup107. This contrasts

36 with the symmetrical localization reported in other organisms. Fusion of spNup96

37 (cytoplasmic localization) with spNup107 (nuclear localization) caused cytoplasmic

38 relocalization of spNup107. In this strain, half of the spNup132 proteins, which interact

39 with spNup107, changed their localization to the cytoplasmic side of the NPC, leading

40 to defects in mitotic and meiotic progression similar to an spNup132 deletion strain.

41 These observations suggest the asymmetrical localization of the outer ring spNup132

42 and spNup120 subcomplexes of the NPC is necessary for normal cell cycle progression

43 in fission yeast.

44

45

Author summary

The nuclear pore complexes (NPCs) form gateways to transport intracellular molecules between the nucleus and the cytoplasm across the nuclear envelope. The Nup107-160 subcomplex, that forms nuclear and cytoplasmic outer rings, is a key complex responsible for building the NPC by symmetrical localization on the nuclear and cytoplasmic sides of the nuclear pore. This structural characteristic was found in various organisms including humans and budding yeasts, and therefore believed to be common among "all" eukaryotes. However, in this paper, we revealed an asymmetrical localization of the homologous components of the human Nup107-160 subcomplex in fission yeast by immunoelectron and fluorescence microscopic analyses: in this organism, the Nup107-160 subcomplex is split into two pieces, and each of the split pieces is differentially distributed to the nuclear and cytoplasmic side of the NPC: one piece is only in the nuclear side while the other piece is only in the cytoplasmic side. This contrasts with the symmetrical localization reported in other organisms. In addition, we confirmed that the asymmetrical configuration of the outer ring structure is necessary for cell cycle progression in fission yeast. This study provides notions of diverse structures and functions of NPCs evolved in eukaryotes.

3

Introduction

In eukaryotes, the nuclear envelope (NE) separates the nucleus from the cytoplasm.

Molecular transport between the nucleus and cytoplasm across the NE occurs through

nuclear pore complexes (NPCs). These complexes are cylindrical, eight-fold

symmetrical structures that perforate the NE and are made of multiple sets of about 30

different protein species known as nucleoporins (Nups) [1–3]. Nups are classified into

three groups: transmembrane Nups, FG repeat Nups, and scaffold Nups.

Transmembrane Nups have transmembrane helices and anchor NPCs to the NE. FG

repeat Nups contain phenylalanine-glycine (FG) rich repeats and are involved in

molecular transport through the NPC cylinder structure. Scaffold Nups form two inner

rings and two outer rings, which serve as the NPC structural core [4–7], and associate

with the membrane through interactions with transmembrane Nups [3,8,9]. These NPC

structures and most Nups are generally conserved among eukaryotes [1,2,10–13],

although numerous species-dependent differences are found [14].

The Nup107-160 subcomplex is a key component of the outer rings and in most

eukaryotes is composed of equal numbers of Nup107, Nup85, Nup96, Nup160,

Nup133, Sec13, and Seh1, and depending on the species Nup37, Nup43, and ELYS are

also included [15–20]. These Nups assemble to form, both *in vitro* and *in vivo*, the Y-

shaped Nup107-160 subcomplex in *Homo sapiens*, the budding yeast *Saccharomyces

cerevisiae,* and the thermophile *Chaetomium thermophilum* [5,20–25]. Nup85, Nup43,

and Seh1 form one of the two short arms, while Nup160, Nup37, and ELYS form the

other. The two arms are connected to Nup96 and Sec13, and Nup96 is connected to

Nup107 and Nup133 to form the long stem (Nup96-Nup107-Nup133) of the Y-shaped

molecule. Multiple copies of the Nup107-160 subcomplex form the outer rings on the

4

92   nucleoplasmic and cytoplasmic sides of the NPC [4,5,26].

93   Like other eukaryotes, the fission yeast *Schizosaccharomyces pombe* has a set of

94   conserved Nups [27–29] (hereafter, we use 'sp' to denote *S. pombe* proteins and 'sc' and

95   'hs' to indicate *S. cerevisiae* and *H. sapiens* proteins). However, the *S. pombe* NPC has

96   several unique features. It contains spEly5 (a potential homolog of metazoan ELYS) and

97   spNup37, but lacks Sec13 and Nup43 [29], and it has two redundant Nup133 homologs

98   (spNup131 and spNup132) in addition to two redundant scNic96/hsNup93 homologs

99   (spNpp106 and spNup97). Most strikingly, the Nup107-160 subcomplex in *S. pombe* is

100   composed of unequal numbers of spNup107, spNup120 (a homolog of hsNup160),

101   spNup85, spNup96, spNup37, spEly5, spSeh1, spNup131 and spNup132 [29]; the

102   relative numbers of spNup107and spNup131 are 4 - 8 in a single NPC, and that of

103   spNup132 is approximately 48 whereas the other components are approximately16.

104   Thus, a unique/different structural organization of the Nup107-160 subcomplex is

105   suggested in *S. pombe* compared with *S. cerevisiae* and humans [29].

106   spNup131 (spNup133a) and spNup132 (spNup133b) have similar molecular

107   structure and both are able to bind to spNup107 [27]. Despite their similar biochemical

108   features, spNup131 and spNup132 are likely to have different functions because gene

109   disruption strains show different phenotypes. The strain lacking spNup132 (*nup132Δ*)

110   displays altered NPC distribution [27]; its growth is inhibited in the presence of

111   thiabendazole (a microtubule-depolymerizing drug) or hydroxyurea (a DNA replication

112   inhibitor) [28,29]; and it exhibits delayed chromosome segregation in meiosis and

113   unusual spore formation [29,30]. The strain lacking spNup131 (*nup131Δ*) doesn't

114   display any of these characteristics. In addition, telomere elongation and deficiency in

115   SUMOylation have been reported in *nup132Δ*-specific phenotypes [31,32]. The causes

116 of these functional differences remain unknown.

117 In the present study, we examined the positioning of each Nup within the NPC in *S.*

118 *pombe* using immunoelectron microscopy and high-precision distance measurements

119 using fluorescence microscopy and found asymmetrical positionings of the outer ring

120 complex components in the nuclear and cytoplasmic sides of the NPC. In addition,

121 genetical alteration of positioning of the key molecule Nup132 of the outer ring

122 subcomplex resulted in the defects observed in *nup132Δ*.

123

Results

125 **spNup131 and spNup132 are differently positioned at the cytoplasmic and**

126 **nucleoplasmic sides of the NPC**

127 The molecular architectures of spNup131 and spNup132 are similar to that found in

128 other species, with an N-terminal β-propeller domain followed by a C-terminal α-helix

129 stack domain [33] (**S1A Fig**). However, phylogenetic analysis indicates that spNup131

130 and spNup132 belong to evolutionarily distant clades, with the spNup131-containing

131 clade branching from a common ancestor of yeast Nup133 homologs much earlier than

132 that of spNup132 (**S1B Fig**). This suggests that despite the similarity in their domain

133 architecture, spNup131 and spNup132 may have structural features that are distinct

134 enough to confer different functions.

135 To understand the differences between spNup131 and spNup132, we examined

136 the positioning of those Nups within the NPC by immunoelectronmicroscopy (IEM).

137 The spNup131 or spNup132 gene was replaced with the respective gene N-terminally

138 fused to GFP (GFP-spNup131 or GFP-spNup132). IEM was carried out using a specific

139 antibody against GFP. The results showed that GFP-spNup131 is located at the

6

140   cytoplasmic side of the NPC, while GFP-spNup132 is located at the nuclear side (**Fig**

141   **1A**). To confirm the accessibility of the nucleus to immunogold particles using this

142   method, the nuclear centromere protein spMis6 [34] was co-stained (**S2A-C Fig**); only

143   the cells positive for spMis6 were evaluated for staining of spNup131(**S2B,C Fig**). A

144   montage picture of spNup131 with quantification shows that spNup131 was exclusively

145   located in the cytoplasmic side of the NPC (left panels of **Fig 1B**). In contrast, the

146   localization of spNup132 was exclusively in the nuclear side (right panels of **Fig 1B**),

147   indicating that spNup131 and spNup132 have distinct localizations. To resolve potential

148   artifacts of GFP-tagging at the N-terminus, we repeated these experiments using strains

149   in which spNup131 and spNup132 were C-terminally fused to GFP. We obtained

150   essentially the same results with N- and C-tagged proteins (**Fig 1C**), suggesting that

151   spNup131 and spNup132 are differentially positioned at the cytoplasmic and nuclear

152   sides, respectively, of the NPC.

153   To confirm the different localization of spNup131 and spNup132 in living cells

154   by fluorescence microscopy (FM), we observed cells simultaneously expressing

155   spNup131 and spNup132 fused with GFP and mCherry, respectively; we also tested

156   cells expressing spNup131 and spNup132 fused with mCherry and GFP, respectively

157   (**Fig 1D**). To determine their localizations within nuclear pores with high-precision, we

158   applied an open-source program "Chromagnon" [35] (This software is available at

159   https://github.com/macronucleus/Chromagnon [36]). After the chromatic correction, the

160   average distance of spNup131 from spNup132 in each nucleus along its radial direction

161   was measured (see Materials and Methods for details). As a result, the position of

162   mCherry-spNup132 relative to GFP-spNup131 was -49.3±1.8 nm (mean±SEM), and the

163   position of mCherry-spNup131 relative to GFP-spNup132 was 32.7±1.4 nm, both

7

164 indicating that spNup131 was located at the exterior position (distant from the nuclear

165 center) compared with the location of spNup132 within the NPC (**Fig 1E**). These results

166 support the interpretation of the IEM observation that spNup131and spNup132 are

167 separately localized in the NPC: spNup131 is positioned at the cytoplasmic side and

168 spNup132 is positioned at the nucleoplasmic side of the NPC.

169

170 **Different functions of spNup131 and spNup132 at the cytoplasmic and**

171 **nucleoplasmic sides of the NPC**

172 To determine the function of spNup131 and spNup132, we identified its interacting

173 proteins using affinity capture/mass spectrometry (**S3A, B Fig**). Several non-Nup

174 proteins that interact with spNup131 and spNup132 were identified (**S3C Fig**).

175 Among the candidate proteins specifically interacting with spNup131, we

176 selected spFar8 (also known as spCsc3) and examined its functional relationship with

177 spNup131. spFar8 is one of the components of the striatin-interacting phosphatase and

178 kinase (STRIPAK) complex [37,38] that regulates the functions of the spindle pole body

179 (SPB; the yeast microtubule-organizing center) during mitosis [39]. GFP-fused spFar8

180 (spFar8-GFP) localized at the nuclear periphery during interphase, as previously

181 reported [39] (see "wild type" in **Fig 2A**). IEM analysis revealed that spFar8-GFP

182 localized at the cytoplasmic side of the nuclear pores (**Fig 2B**). This NPC localization of

183 spFar8-GFP was greatly decreased in the *nup131Δ* cells (see "*nup131Δ*" in **Fig 2A**) but

184 not in the *nup132Δ* cells ("*nup132Δ*" in **Fig 2A)**. Western blotting analysis of the cell

185 strains tested above showed no marked changes in the amount of spFar8 protein (**Fig**

186 **2C**). The mislocalization of spFar8 in the *nup131Δ* cells occurred when spNup132 was

187 ectopically expressed, whereas normal localization was restored when spNup131 was

8

188   expressed (**Fig 2D, E**). Localization of another STRIPAK complex protein, spFar11, to

189   the nuclear periphery was also decreased in *nup131Δ* cells (**S4 Fig**). These results

190   suggest that spNup131 plays a role in retaining the STRIPAK complex at the

191   cytoplasmic side of the NPC in interphase cells. The genetic interaction of STRIPAK

192   proteins with spNup131 shown by this experiment is consistent with their localization at

193   the cytoplasmic side of the NPC indicated by IEM.

194   Among the candidate spNup132 interacting proteins identified by affinity

195   capture/mass spectrometry (**S3C Fig**), we examined the functional relationship of

196   spNup211 with spNup132. spNup211 is an *S. pombe* homolog of human Tpr and *S.*

197   *cerevisiae* Mlp1 and Mlp2 [40]; Tpr homologs are known to localize on the nuclear side

198   of the NPC [41,42]. IEM analysis of spNup211 showed that spNup211-GFP localized at

199   the nuclear side of the nuclear pores as expected (**Fig 3A**). To examine its localization in

200   relationship to spNup132, GFP-fused spNup211 (spNup211-GFP) was observed by FM

201   in wild type, *nup131Δ*, and *nup132Δ* cells. In wild type and *nup131Δ* cells, spNup211-

202   GFP was localized at the nuclear periphery (see "wild type" and "*nup131Δ*" in **Fig 3B**).

203   In contrast, in the *nup132Δ* cells, spNup211-GFP formed several bright foci at the

204   nuclear periphery ("*nup132Δ*" in **Fig 3B**). We measured the maximum fluorescence

205   intensity of spNup211-GFP in each nucleus in wild type, *nup131Δ*, and *nup132Δ* cells.

206   The value was significantly higher in the *nup132Δ* cells (**Fig 3C, left graph**) whereas

207   spCut11-mCherry, as a control, was uniformly distributed at the nuclear periphery with

208   similar maximum fluorescence intensities in all strains (**Fig 3C, right graph**). This

209   result suggests that the distribution of spNup211 at the NPC is regulated specifically by

210   spNup132 but not spNup131. This fact is consistent with their localizations at the

211   nucleoplasmic side of the NPC, and the lack of interaction between spNup211 and

212 spNup131 is also consistent with their different localizations within the NPC.

213

214 **Immunoelectron microscopy of spNup107-160 subcomplex Nups**

215 Because the Nup133 homologs are integrated components of the Nup107-160

216 subcomplex, we next examined the positioning of the other Nup107-160 subcomplex

217 components in *S. pombe*: spNup107 (scNup84/hsNup107), spNup120

218 (scNup120/hsNup160), spNup85 (scNup85/hsNup85), spNup96 (also known as

219 spNup189C; scNup145C/hsNup96), spNup37 (hsNup37), spEly5 (hsELYS), and

220 spSeh1 (scSeh1/hsSeh1) in cells expressing each of these Nups fused to GFP. A

221 spNup98-spNup96 fusion protein is expressed as the *nup189*[+] gene product, and

222 spNup96 is generated by cleavage with the autopeptidase activity in the C-terminus of

223 spNup98 [43].

224 IEM results showed that of the 7 Nups, spNup120, spNup85, spNup96,

225 spNup37, spEly5, and spSeh1 were predominantly located on the cytoplasmic side of

226 the NPC, whereas spNup107 was located on the nuclear side of the NPC (**Fig 4A**). The

227 localization of spNup107 on the nuclear side was also confirmed using an N-terminus

228 fusion protein (**Fig 4A**). Simultaneous detection of spMis6-GFP further confirmed the

229 localization of spNup120, spNup85, spNup96, spNup37, spEly5 and spSeh1 on the

230 cytoplasmic side of the NPC (**Fig 4A**). This result suggests that the Nup107-160

231 subcomplex is split into two pieces in *S. pombe* and that these two pieces are

232 differentially located on the cytoplasmic and nuclear sides of the NPC. This result

233 contrasts with the structure of the Nup107-160 complex reported in *S. cerevisiae* and

234 humans, in which all of the components are connected to form the Y-shape structure.

235 Thus, this result suggests an unexpected separation of the Nup107-160 subcomplex at

236   the junction of spNup96 and spNup107 in *S. pombe*.

237   To confirm the different localizations of the Nup107-160 subcomplex

238   components by FM, we examined the localization of these components in living cells.

239   We chose spNup85 and spNup107 as representatives of cytoplasmic and nucleoplasmic

240   components identified by IEM. We first determined the position of spNup85-GFP

241   within NPCs by comparing it with that of mCherry-spNup131 and mCherry-spNup132

242   (**Fig 4B**). The position of mCherry-spNup131 relative to spNup85-GFP was 11.4±1.9

243   nm (mean±SEM) and the position of mCherry-spNup132 relative to spNup85-GFP was

244   -26.2±1.0 nm (**Fig 4B**; the relative position of Nup85 to Nup131 and Nup132 is

245   indicated in the right panel). This result supports cytoplasmic positioning of spNup85 as

246   indicated by IEM. Second, we determined the position of spNup107-GFP within NPCs

247   using a similar method. The position of mCherry-spNup131 relative to spNup107-GFP

248   was 34.0±2.1 nm and the position of mCherry-spNup132 relative to spNup107-GFP was

249   -4.4±1.0 nm (**Fig 4C**; the relative position of Nup107 to Nup131 and Nup132 is

250   indicated in the right panel). This result supports nuclear positioning of spNup107 as

251   indicated by IEM.

252   Taken together, these results demonstrate that the Nup107-160 subcomplex

253   components are differentially localized at the cytoplasmic and nucleoplasmic sides

254   within the NPC in *S. pombe* (**Fig 4D**). Thus, we call hereafter the cytoplasmic

255   components (spNup131, spNup120, spNup85, spNup96, spNup37, spEly5 and spSeh1)

256   as the spNup120 subcomplex and the nucleoplasmic components (spNup132 and

257   spNup107) as the spNup132 subcomplex.

258   Based on the localization analysis in this study and quantification of each Nup

259   reported previously [29], we estimated the molecular weight of the cytoplasmic outer

11

260   ring (composed of the spNup120 subcomplex) and nucleoplasmic outer ring (composed

261   of the spNup132 subcomplex) as 7.4 MDa and 7.0 MDa, respectively: the cytoplasmic

262   outer ring is estimated as 8-fold of a single unit (two each of spNup120, spNup85,

263   spNup96, spEly5, and spNup37 and one each of spSeh1 and spNup131), and the

264   nucleoplasmic outer ring is estimated as 8-fold of a single unit (six spNup132 and one

265   spNup107). In this estimation, a single unit of both the cytoplasmic and nucleoplasmic

266   outer rings consist of 7 α-solenoids and 6 β-propellers as elements, suggesting that

267   similar ring structures may be consequently built in both sides. The values are a bit

268   larger than the molecular weight (4.65 MDa) of one outer ring in *S. cerevisiae*, which

269   consists of 8-fold of a single unit containing 5 α-solenoids and 4 β-propellers as

270   elements [26].

271

272   **Enforced cytoplasmic localization of Nup107 by fusing to Nup96 results in**

273   **reduction of Nup132 from the nuclear side, leading to defects in meiosis**

274   To address the significance of the separated localization of the Nup107-160

275   subcomplex, we generated an *S. pombe* strain with spNup96 (one of the cytoplasmic

276   outer ring Nup120 subcomplex components) artificially fused to spNup107 (one of the

277   nuclear outer ring Nup132 subcomplex components) in a *nup107Δ* background

278   (spNup96-spNup107-GFP). The strain was viable, and Western blot analysis confirmed

279   expression of the fusion protein with the predicted molecular weight (**Fig 5A**). By IEM,

280   the majority of the spNup96-spNup107-GFP fusion protein molecules were localized at

281   the cytoplasmic side of the NPC (**Fig 5B**), showing a change in the location of

282   spNup107 from the nuclear side to the cytoplasmic side. Under this condition,

283   spNup132 was recruited to both the nuclear and cytoplasmic sides of the NPC (**Fig 5C**),

284   suggesting that a significant fraction of the spNup132 molecules was recruited by

285   spNup107. We assumed that the cytoplasmic recruitment of spNup132 molecules would

286   result in a reduction of spNup132 at the nuclear side. As previously reported, the

287   *nup132Δ* cells exhibit growth sensitivity to the microtubule-destabilizing drug

288   thiabendazole (TBZ), and they have delayed meiotic division and abnormal spore

289   formation [28–30]. Thus, we examined whether the spNup96-spNup107-GFP strain

290   showed those deficiencies. We found that this strain exhibited growth sensitivity to TBZ

291   (**Fig 5D)**, delayed meiotic division (**Fig 5E, F**), and abnormal spore formation (**Fig 5G**),

292   similarly to the defects found in *nup132Δ* cells. This result suggests that these defects

293   are caused by reduction in the number of spNup132 located at the nuclear outer ring of

294   the NPC, and also suggests that concomitant localization of spNup107 and a part of

295   Nup132 with the spNup120 subcomplex at the cytoplasmic side of the NPC caused

296   defects in normal progression of mitosis and meiosis. Thus, split structure and

297   asymmetrical localization of the Nup107-160 subcomplex are necessary for the normal

298   progression of mitosis and meiosis in *S. pombe*.

299

300   **The N-terminal β-propeller region is required for differential localization of**

301   **Nup133 homologs**

302   Finally, we determined which domains of spNup131 and spNup132 were responsible for

303   their different localizations. In this experiment, we expressed full length spNup131 or

304   spNup132, fragments of spNup131 or spNup132, or chimeric proteins of spNup131 and

305   spNup132 (**Fig 6A**). To exclude the possibility that endogenous spNup131 or spNup132

306   predominantly occupy preferred sites for spNup131 and spNup132 fragments or

307   chimeric proteins, a *nup131Δ nup132Δ* double-deletion strain (lacking genes for both

13

308 spNup131 and spNup132) was used. Protein expression was confirmed by Western blot

309 analysis (**S5 Fig**). FM observation showed that GFP fused full-length spNup131

310 (spNup131FL) and spNup132 (spNup132FL) were localized at the nuclear periphery

311 (**Fig 6B**). The N-terminal domains of both Nup131 and Nup132 (spNup131N and

312 spNup132N) were not localized at the nuclear periphery, while the C-terminal domain

313 of both proteins (spNup131C and spNup132C) were localized at the nuclear periphery,

314 consistent with a previous report [44]. Interestingly, IEM analysis showed that

315 spNup131C localized to the nuclear side of the NPC (**Fig 6C**) in contrast with the

316 localization of full length spNup131 on the cytoplasmic side (compare the upper two

317 panels in **Fig 6C**; also see **Fig 1B**). These results suggest that the C-terminal domains of

318 both spNup131 and spNup132 have the ability to localize on the nuclear side of the

319 NPC, probably through binding to Nup107, and also suggest that the N-terminal

320 domains of spNup131 and spNup132 are involved in determining their differential

321 localizations. To test this idea, we examined the localization of the chimeric proteins

322 spNup131N+spNup132C and spNup132N+spNup131C: If the C-terminal domains were

323 independent and functioning correctly, both chimeric proteins should be localized to the

324 nuclear side of the NPC via interaction with Nup107, and if the N-terminal domains

325 were independent and functioning correctly, the spNup131N+spNup132C protein

326 should then be localized to the cytoplasmic side via Nup131N and the

327 spNup132N+spNup131C protein should be retained on the nuclear side via Nup132N.

328 The results showed that the spNup131N+spNup132C chimeric protein mostly diffused

329 to the cytoplasm with some enrichment in the nuclear periphery compared with

330 spNup132FL (**Fig 6B**) and that the other chimeric protein, spNup132N+spNup131C,

331 also diffused to the cytoplasm but with no enrichment in the nuclear periphery

14

332   compared with spNup131FL (**Fig 6B**). The relatively strong cytoplasmic staining of the

333   chimeric proteins suggests that the N-terminal domains may function to prevent

334   "abnormal" localization of spNup131 and spNup132. Overall, this result indicates that

335   both N-terminal and C-terminal domains are required for the proper differential

336   localization of spNup131 and spNup132.

337

338   **Immunoelectron microscopy of the other nucleoporins**

339   Because the Nup107-160 subcomplex seems to have a unique organization in *S. pombe,*

340   we wished to understand the overall structure of the NPC. For this purpose, we

341   performed IEM of other Nups to reveal their positionings within the NPC. GFP-fused

342   Nups were used and IEM was carried out using a specific antibody against GFP, unless

343   specified otherwise (**Fig 7**). We first examined inner ring Nups known as the Nup93

344   subcomplex in vertebrates. spNup97 and spNpp106, redundant *S. pombe* homologs of

345   scNic96/hsNup93, were both similarly positioned near the center of the NPC (**Fig 7A**);

346   the redundancy of scNic96/hsNup93 homologs is unique to the *Schizosaccharomyces*

347   genus. spNup184 (scNup188/hsNup188) and spNup186 (scNup192/hsNup205) were

348   also positioned near the center (**Fig 7A**). spNup40 (scNup53/scNup59/hsNup35) and

349   spNup155 (scNup157/scNup170/hsNup155) were also located near the center of the

350   NPC, but they showed a slightly broader range of localization (**Fig 7A**).

351   The channel Nups spNup44 (scNup57/hsNup54) and spNup45

352   (scNup49/hsNup58) were positioned at the center of the pore (**Fig 7B**). spNup98

353   (scNup145n/hsNup98) was detected on the cytoplasmic side of the nuclear pore when

354   using an anti-GFP antibody (see "spNup98-GFP" in **Fig 7B**); however, an anti-Nup98

355   antibody (clone 13C2) [45], which specifically recognizes endogenous spNup98,

15

356   detected its positioning near the center of the pores (see "spNup98" in **Fig 7B**). This

357   staining pattern is likely due to the interaction of spNup98 with other Nups. In *H.*

358   *sapiens* and *S. cerevisiae*, the C-terminal region of the Nup98 homologs

359   (hsNup98/scNup145n/scNup100/scNup116) interacts with Nup96 homologs

360   (hsNup96/scNup145c) [46–49], and the C-terminal Nup98-APD (autoproteolytic and

361   NPC-targeting domain) binds to Nup88 homologs (hsNup88/scNup82) and to Nup96 in

362   a mutually exclusive manner [49]. Thus, the C-terminal region of spNup98 might be

363   tethered by spNup96 and spNup82, both of which are positioned at the cytoplasmic side

364   of the NPC, while the N-terminal region is extended to the center of the pore. The *S.*

365   *pombe* homolog of the conserved Nup Nsp1 (scNsp1/hsNup62) was localized

366   frequently in the cytoplasmic side and infrequently in the nuclear side of the NPC (**Fig**

367   **7B**).

368   spNup82 (scNup82/hsNup88) and spNup146 (scNup159/hsNup214) were

369   detected at the cytoplasmic side (**Fig 7C**) as expected from their homologous

370   counterparts. spAmo1(scNup42/hsNlp1) was also detected at the cytoplasmic side (**Fig**

371   **7C**). The transmembrane Nups, spCut11 (scNdc1/hsNdc1), spPom152 (scPom152), and

372   spPom34 (scPom34) were localized at the center of the pore and slightly biased toward

373   the cytoplasm (**Fig 7D**). The conserved Nups, spNup60 (scNup60), spNup61

374   (scNup2/hsNup50), and spNup124 (scNup1/hsNup153) (**Fig 7E)** as well as

375   spNup211(scMlp1/scMlp2/hsTpr) (**Fig 3A**) were detected at the nuclear side as

376   expected from their homologous counterparts. We added a recently identified Nup

377   spAlm1 [50] to the group of nuclear Nups, according to its nucleoplasmic localization

378   **(Fig 7E)**.

379   We summarized the positionings of the *S. pombe* Nups within the NPC in **Fig**

16

380   **8**. Transmembrane Nups (spCut11, spPom152, and spPom34); inner ring Nups

381   (spNup97, spNpp106, spNup184, spNup186, spNup40, and spNup155); cytoplasmic

382   ring Nups (spNup82, spNup146, spAmo1, spNsp1); central channel Nups (spNsp1,

383   spNup98, spNup44, and spNup45); and nuclear basket Nups (spNup124, spNup60,

384   spNup61, spNup211, and spAlm1) are positioned similarly to the positions of their

385   orthologs in *S. cerevisiae* and human [1,4,5,26,51]. Thus, these NPC substructures,

386   which include a central channel structure that is required for nucleocytoplasmic

387   transport, seem to be common to other eukaryotes. In contrast, the outer ring Nup107-

388   160 subcomplex (spNup131, spNup120, spNup85, spNup96, spNup37, spEly5 and

389   spSeh1, spNup107 and spNup132) in *S. pombe* has a highly unusual asymmetrical

390   organization: It splits into two pieces (spNup120 and spNup132 subcomplexes). The

391   spNup120 subcomplex (spNup131, spNup120, spNup85, spNup96, spNup37, spEly5

392   and spSeh1) is located in the cytoplasmic side of the NPC while the spNup132

393   subcomplex (spNup107 and spNup132) is located in the nuclear side of the NPC. This

394   asymmetrical organization of the Nup107-160 subcomplex may be required for building

395   and maintaining the structural organization of the central channel and other NPC

396   elements common to other eukaryotes, and consequently, the Nup107-160 subcomplex

397   would be required for normal cell cycle progression in *S. pombe.*

398

399   **Discussion**

400   IEM of *S. pombe* Nups suggest that the *S. pombe*-specific Nup107-160 subcomplex

401   structure is uniquely split into two pieces that localize differentially to the cytoplasmic

402   and nuclear sides of the NPC while preserving the conserved modular structures of the

403   Nup107-160 subcomplexes of other eukaryotes. High-precision distance measurements

17

404   using FM also support this result (**Fig 1D, E, and 4b**). The asymmetrical organization

405   of the *S. pombe* Nup107-160 subcomplex contrasts with the localization of the Nup107-

406   160 subcomplexes in *H. sapiens*, *S. cerevisiae* and *Trypanosoma brucei*, in which

407   Nup107-160 complexes are found on both the cytoplasmic and nuclear sides of the NPC

408   [1,5,13,26,52]. Our results suggest that the *S. pombe* NPC has a novel organization that

409   has evolved in the *Schizosaccharomyces* genus, which commonly bears the Nup132 and

410   Nup131 clades (**S1B Fig**).

411   In *H. sapiens* and *S. cerevisiae,* the Nups in the Nup107-160 subcomplex

412   assemble to form Y-shaped structures [5,21,24,25,53]. A total of 32 Y-complexes form

413   two concentric reticulated rings at both the nuclear and cytoplasmic sides of the human

414   NPC [4,5]. This organization may be supported by the iso-stoichiometry of each Nup in

415   the Nup107-160 subcomplex: the amounts of each Nup in the Nup107-160 subcomplex

416   in human cells are nearly equal [54]. In contrast, in *S. pombe*, the amounts of each Nup

417   in the Nup107-160 subcomplex are not equal but highly divergent, ranging from 1 copy

418   to 5-6 copies/unit [29]. In addition, the Sec13 homolog in *S. pombe* does not localize in

419   the NPC, and Nup43 is not conserved in the genome [29]. The different stoichiometry

420   and composition of the *S. pombe* Nup107-160 subcomplex components are likely due to

421   the unique fission yeast–specific separated structure of the Nup107-160 subcomplex

422   revealed in this study.

423   Two Nup133 homologs spNup131 and spNup132 play different roles with

424   different positions at the NPC. spNup132 is required for normal kinetochore formation

425   during meiosis in *S. pombe* [30]. Deletion of the *nup132* gene but not the *nup131* gene

426   causes untimely kinetochore assembly and activates spindle assembly checkpoint

427   machinery during the first meiotic chromosome segregation [30]. The deletion of the

18

428   *nup132* gene also increases the sensitivity to the microtubule-destabilizing drug

429   thiabendazole, likely due to defects in the kinetochore structure in mitosis [29].

430   Similarly, in mammalian cells, kinetochore-related functions have been reported for the

431   Nup107-160 subcomplex. A fraction of the Nup107-160 subcomplex is found at the

432   kinetochores and spindle poles during mitosis [16,17,55,56], and depletion of the

433   Nup107-160 subcomplex from kinetochores results in altered kinetochore protein

434   recruitment [57–59]. While the molecular mechanism of underlying spNup132-

435   mediated regulation of kinetochore proteins remains unknown, considering the

436   similarity in kinetochore-related functions, spNup132, but not spNup131, is likely to be

437   a functional homolog of mammalian Nup133.

438   On the other hand, spNup131 plays a different role at the cytoplasmic side of

439   the NPC. IEM analysis in this study revealed that spNup131 is localized only on the

440   cytoplasmic side of the NPC, and a genetic analysis showed interaction between

441   spNup131 and spFar8. spFar8, which was proven to be located at the cytoplasmic side

442   of the NPC in this study, is an *S. pombe* ortholog of the STRIPAK complex component

443   Striatin [38]. In *S. pombe*, the STRIPAK complex regulates the septation initiation

444   network through the conserved protein kinase Mob1 [37,60] and is required for

445   asymmetric division of mother and daughter SPBs during mitosis [39]. The spNup131-

446   dependent NPC localization of spFar8 revealed by this study implies that the NPC

447   regulates STRIPAK localization in interphase cells. Human STRIPAK complexes have

448   been proposed to play roles at the interface between the Golgi and the outer nuclear

449   envelope [38]. Considering the physical and genetic interaction with spNup131,

450   STRIPAK is likely to interact with the NPC on the cytoplasmic side of the NE.

451   Although the role of the STRIPAK complex in interphase cells in *S. pombe* is not fully

19

452 understood, the interaction between spNup131 and spFar8 may provide an important

453 example linking the NPC to cytoplasmic structures.

454   This study demonstrates that the *S. pombe* Nup107-160 subcomplex has a

455 novel separated structure and exhibits a localization pattern not reported in other

456 organisms. Recent studies suggest that NPC structures are not necessarily the same

457 among eukaryotes [26,61,62]. For example, the binucleated ciliate *Tetrahymena*

458 *thermophila,* a single-cell organism, has two functionally distinct nuclei, the

459 macronucleus (MAC) and micronucleus (MIC), in a single cell: The MAC and MIC

460 differ in size, transcriptional activity, and nucleocytoplasmic transport specificity [63].

461 Interestingly, in *T. thermophila,* the MAC and the MIC NPCs are composed of differ

462 amounts of the Nup107-160 subcomplex components [61]. The amount of the

463 subcomplex in the MIC is about three times more than that in the MAC, suggesting that

464 the Nup107-160 subcomplex forms different structures in the MAC from the MIC. In

465 the green algae *Chlamydomonas reinhardtii*, a single cell organism, the NPCs have 24

466 subcomplexes asymmetrically distributed within a single NPC: 16 at the nuclear side

467 forming double outer rings and 8 at the cytoplasmic side forming one outer ring [62].

468 The asymmetrical distribution of the Nup107-160 subcomplex in *C. reinhardtii* may

469 suggest a specific function of the complex in either cytoplasmic or nuclear side of the

470 NPC although it is currently unclear. In some multicellular organisms, the expression

471 level of Nups varies between cell types and during development [54,64–67]. It is also

472 known that some mutations in Nups result in developmental defects in metazoans [68].

473 These findings suggest that the NPC composition in cell types and during development

474 is biologically significant. Altered compositions might alter the NPC structure, at least

475 in part; thus, unidentified NPC subcomplex structures may play roles in specific

476   biological events such as differentiation and development. Thus, we speculate that novel

477   NPC structures may be important to elucidate the biological functions of the NPC.

478

479   **Materials and Methods**

480   *S. pombe cell cultivation*

481   Strains used in this study are listed in S1 Table. YES or EMM2 culture medium was

482   used for routine cultures [69]. ME medium was used to induce meiosis and spore

483   formation. When necessary, TBZ (T5535-50G, Sigma-Aldrich Inc, Tokyo, Japan) was

484   added to the YES medium to a final concentration of 10 μg/mL.

485

486   *Immunoelectron microscopy*

487   For immunoelectron microscopy, 1.5×10^8 cells expressing GFP-Nup131 were fixed in

488   1 mL of a mixture of 4% formaldehyde (18814-10, Polysciences, Inc, Warrington, PA,

489   USA) and 0.01% glutaraldehyde (1909-10, Polysciences, Inc.) dissolved in 0.1 M

490   phosphate buffer (PB) (pH 7.4) for 20 min at room temperature, treated with 0.5 mg/mL

491   Zymolyase 100T (7665-55, Nacalai Tesque, Inc., Kyoto, Japan) in PB for 20-30 min at

492   30°C, and then permeabilized with 0.2% saponin (30502-42, Nacalai Tesque, Inc.) and

493   1% bovine serum albumin (BSA) in PB for 15 min. The GFP epitope tag was labeled

494   with a primary antibody (600-401-215, rabbit polyclonal anti-GFP antibody, Rockland

495   Immunochemicals, Limerick, PA, USA) diluted 1:400 in PB containing 1% BSA and

496   0.01% saponin, and a secondary antibody (7304, goat anti-rabbit Alexa 594

497   FluoroNanogold Fab' fragment; Nanoprobes Inc., Yaphank, NY, USA) diluted 1:400.

498   The same immunostaining conditions were used for the cells expressing each of the

499   other GFP-fused Nups except for the dilution ratios of primary and secondary

21

500 antibodies; the conditions used for each experiment are listed in S2 Table. For analysis

501 of the spNup98 N-terminal region, we used a mouse monoclonal anti-Nup98 antibody

502 (13C2) [43,45] (available from BioAcademia Inc, Japan, Cat. #70-345) diluted 1:100

503 and anti-mouse Alexa594 FluoroNanogold Fab' fragment (7302, Nanoprobes) diluted

504 1:400. Cells then were fixed again with 1% glutaraldehyde in PB for 1 h at room

505 temperature and treated with 100 mM lysine HCl in PB twice for 10 min each. The cells

506 were stored at 4°C until use. Before use, the cells were incubated with 50 mM HEPES

507 (pH 5.8) three times for 3 min each and with distilled water (DW) once, incubated with

508 Silver enhancement reagent (a mixture of equal volumes of the following A, B, and C

509 solutions: A, 0.2% silver acetate solution; B, 2.8% trisodium citrate-$2H_2O$, 3% citric

510 acid-H_2O, and 0.5% hydroquinone; C, 300 mM HEPES, pH 8.2) at 25°C for 2-5 min.

511 Cells were embedded in 2% low melting agarose dissolved in DW. Cells were post-

512 fixed with 2% OsO_4 in DW for 15 min and stained with 1% uranyl acetate in DW at

513 room temperature. Cells were dehydrated using stepwise incubations in ethanol and

514 acetone and finally embedded in epoxy resin Epon812. Solidified blocks containing

515 cells were sectioned, and the ultra-thin sections were stained with uranyl acetate and

516 lead citrate, the usual pretreatment for EM observations. Images were obtained using a

517 JEM1400 transmission electron microscope (JEOL, Tokyo, Japan) at 120kV.

518   Nuclear pores containing more than two immunogold particles were chosen for

519 localization analysis as described previously [1]. To confirm the accessibility of the

520 nucleus to immunogold particles, the nuclear centromere protein spMis6-GFP was co-

521 expressed with GFP-fused Nups in cells and stained with anti-GFP antibody for IEM.

522 For quantification of the Nup signals, we chose only cell specimens with a positive

523 spMis6-GFP signal. For quantitative representations, montage pictures were produced

22

524   by stacking 20 NPC images with 5% opacity on Adobe Photoshop CS software.

525

526   ***cDNA clones***

527   *nup107$^+$* and *nup37$^+$* cDNAs were provided by National BioResource Project Japan

528   (http://yeast.lab.nig.ac.jp/yeast/top.xhtml). cDNA fragments of other Nups were

529   amplified from a cDNA library pTN-RC5 or pTN-FC9 (National BioResource Project

530   Japan) using PCR.

531

532   ***Strain construction***

533   To visualize nuclear pore localization of the different domains of Nup131 and Nup132,

534   *lys1$^+$*-integrating plasmids carrying GFPs65t-fused with respective Nup domains were

535   introduced into cells with a *nup131Δnup132Δ* double-deletion mutant background. To

536   construct the spNup96-spNup107 fusion Nup, a cDNA fragment encoding spNup107 or

537   spNup107-GFP followed by a drug resistance marker gene was integrated after the

538   chromosomal spNup96 coding region. After a diploid strain was obtained by crossing

539   the spNup96-spNup107 fusion containing strain with the wild type strain, the *nup107$^+$*

540   gene on the original chromosomal locus was deleted. To introduce the chromosomal

541   fluorescent tag and gene disruption, a two-step PCR method was applied [70]. Nup-GFP

542   fusion constructs were described previously [29]. The spMis6-GFP fusion was

543   constructed as described previously [71] or using the two-step PCR method. mCherry-

544   spAtb2 was visualized as described previously [30].

545

546   ***Plasmid construction***

547   To express the full-length or domains of the spNup131 and spNup132 proteins, cDNA

23

548   fragments were amplified by PCR. For overexpression, the PCR products were sub-

549   cloned into the plasmid that carries the *nmt1* promoter and terminator. For physiological

550   expression, the PCR products were sub-cloned into the *Bgl*II site of the plasmid (pY53)

551   that carries the *nup132* promoter (-1000bp)-driven GFPs65t and the *nmt1* terminator.

552   Each sub-cloning was done by using the In-Fusion PCR cloning kit (Clontech

553   Laboratories, Mountain View, CA, USA). Plasmids were integrated at the *lys1* gene

554   locus. Correct integrations were confirmed by PCR.

555

556   ***Fluorescence microscopy***

557   Images were obtained using a DeltaVision microscope system (GE Healthcare, Tokyo,

558   Japan) equipped with a CoolSNAP HQ^2 CCD camera (Photometrics, Tucson, AZ, USA)

559   through an oil-immersion objective lens (PlanApoN60×OSC; NA, 1.4) (Olympus,

560   Tokyo, Japan) as described previously [29]. Z-stack images were obtained and

561   processed by deconvolution and denoising algorithm [72] when necessary. For time

562   lapse microscopy, cells were observed every 5 minutes as described previously [30].

563   The projection images of z-stacks were made by softWoRx software equipped in the

564   microscope system.

565

566   ***Precise distance measurements with fluorescence microscopy***

567   Cells to be analyzed were cultured in 150 µl of the EMM2 5S medium on an 8-well

568   chambered coverglass, Lab-Tek II (Thermo Fisher Scientific Japan, Yokohama, Japan);

569   cells used for references for chromatic correction were also cultured in a chamber of the

570   same coverglass. Simultaneously acquired multicolor images were obtained with OMX

571   SR (GE Healthcare) equipped with three sCMOS cameras. The three-dimensional (3D)

24

572   images were deconvolved by constrained iterative deconvolution using the Priism suite

573   (http://msg.ucsf.edu/IVE/) with a Wiener filter enhancement of 0.9 and 15 iterations. To

574   correct for chromatic shifts of multicolor FM images, green-to-red photoconversion of

575   GFP was used as the reference as previously reported [73,74]: Nup96-GFP was used in

576   this study. For photoconversion, cells were illuminated with 405 nm light at about 393

577   W/cm^2 for 4 seconds, then both green and red-converted GFP species were excited with

578   488 nm to obtain images of the same object in the green and red channels. Chromatic

579   shifts were measured using such images, and the correction parameters were determined

580   using the Chromagnon software (https://github.com/macronucleus/Chromagnon), by

581   which a chromatic shift can be corrected with an accuracy of ~10 nm in 2D XY plane

582   and ~15 nm in 3D XYZ space using test samples [35]. The correction parameters were

583   applied to all images obtained from the same chambered coverglass as described in [35].

584   Next, individual nuclei in the images were identified and segmented by our

585   software using functions from the "ndimage" module of the Scipy package

586   (http://www.scipy.org). The centers of the nuclei were identified by least-square fitting

587   with 3D ellipses using the 3D coordinates of the nucleoporin fluorescence above

588   threshold. The images of the NE at the midsection were linearized with polar

589   transformation. These images were then averaged across all angles to produce 1D

590   intensity profiles along the radial direction of the nuclei. The intensity profiles were

591   fitted to Gaussian profiles to determine a distance between the peaks of green and red

592   for each of the individual nuclei. The mean distance was determined from more than 70

593   nuclei. Because not all nuclei were round, we rejected nuclei of elliptical or irregular

594   shapes before the final calculation.

595

25

596 *Western blot analysis*

597 For western blot analysis, whole cell extracts were prepared from approximately 5×10^6

598 cells by trichloroacetic acid (TCA) precipitation as described previously [29]. To detect

599 GFP-fused proteins, a rabbit polyclonal anti-GFP antibody (600-401-215, Rockland

600 Immunochemicals Inc.) was used. To detect spNup98, a mouse monoclonal anti-Nup98

601 antibody (13C2) was used [45]. HRP-conjugated goat anti-rabbit or anti-mouse IgG

602 (NA9340-1ml or NA9310-1ml, GE Healthcare) was used as a secondary antibody.

603 Protein bands were detected by chemiluminescence using ChemiDoc MP imaging

604 system (Bio-Rad).

605

606 *Preparation of whole cell extracts for affinity-capture experiments*

607 Growing cells (about 5×10^9) were collected and washed with 10 mM HEPES buffer

608 (pH 7.5) containing 1 mM phenylmethylsulfonyl fluoride (PMSF). The washed cells

609 were divided into aliquots of 3×10^8 cells in 10 mM HEPES buffer (pH 7.5) containing

610 1 mM PMSF. Cells were again collected by centrifugation, and the cell pellet was kept

611 frozen by liquid nitrogen until use. To make a cell extract, the cell pellet was thawed

612 and suspended in 100 μL of lysis buffer (50 mM HEPES (pH 7.5), 150 mM NaCl, 1%

613 Triton X-100, 1 mM EDTA, 2 mM PMSF) with a protease inhibitor cocktail (165-

614 20281, Wako, Tokyo, Japan) and mashed by glass beads using Multi-beads shocker

615 (Yasui Kikai Corporation, Osaka, Japan). We chose this extraction condition based on a

616 previous study identifying the components of plant NPCs [11]. Because the presence of

617 1% Triton X-100 gave better results for extracting plant NPC components, we decided

618 to use 1% Triton X-100 as a detergent, and we examined three different salt conditions

619 (50 mM, 150 mM or 500 mM NaCl) in the presence of the detergent. As a result, 150

620   mM NaCl gave better results with low background. At least for extracting spNup131

621   and spNup132, this condition was better than that optimized for extracting NPCs in

622   other organisms such as budding yeast (1.5 M ammonium acetate, 1% Triton X-100)

623   [75] and trypanosoma (20 mM HEPES (pH7.4), 250 mM NaCitrate, 0.5% Triton X-100,

624   0.5% deoxy Big CHAP) [76]. After further addition of 400 μL of lysis buffer, the

625   mashed cell pellet was transferred to new microtubes. The supernatant was collected

626   after centrifugation at 15000 rpm for 15 min at 4°C and used as the whole-cell extract.

627

628   *Affinity-capture and LC/MS/MS analysis*

629   The whole-cell extract was incubated with a rabbit anti-GFP antibody (600-401-215,

630   Rockland Immunochemicals). Antibody-conjugated proteins were collected by

631   incubating with Protein A Sepharose beads (17528001, GE Healthcare). Beads were

632   then washed 4-5 times with the lysis buffer described above. After elution in SDS-

633   PAGE sample buffer, protein samples were loaded onto a 12% SDS-PAGE gel for liquid

634   chromatography coupled to tandem MS (LC/MS/MS). Data analysis for LC/MS/MS

635   was performed as described previously [77] using the Pombase protein dataset released

636   on November 12th, 2015. To identify proteins interacting with spNup131 and spNup132,

637   protein samples were prepared from two independent experiments and each preparation

638   was analyzed by LC/MS/MS. Proteins detected as more than one unique spectrum were

639   identified as interacting proteins with spNup131 and spNup132. Alternatively, when

640   proteins detected as only one unique spectrum in the first experiment were repeatedly

641   detected in the second experiment, they were also identified as interacting proteins.

642

643   **Acknowledgments**

27

644   We thank Naomi Takagi for technical assistance for mass spectrometry analysis and the

645   National BioResource Project Japan for the Nup cDNA clones. We also thank Drs.

646   Thomas U. Schwartz, Valérie Doye, and David B Alexander for critical reading of this

647   paper.

648

649   **Competing financial interests**

650   The authors declare no competing financial interests.

651

652   **Supporting information**

653   **S1 Fig.** Phylogenetic analysis of Nup133 proteins

654   **S2 Fig.** IEM images of spMis6-GFP, GFP-spNup131, and GFP-spNup132

655   **S3 Fig.** Affinity capture/mass spectrometry of GFP-spNup131 and GFP-spNup132

656   **S4 Fig.** FM images of spFar11-GFP in wild type, *nup131Δ*, and *nup132Δ* cells.

657   **S5 Fig.** Detection of GFP fused protein fragments by Western blot.

658   **S1 Table.** *S. pombe* strains used in this study

659   **S2 Table.** Dilution ratios of primary and secondary antibodies used for IEM

660   **S1 Dataset.** Individual IEM images of 20 NPCs used for superimposed images of Fig 1C

661   (spNup131-GFP and spNup132-GFP)

662   **S2 Dataset.** Values of the distance between mCherry-spNup132 and GFP-spNup131 and

663   those between mCherry-spNup131 and GFP-spNup132 measured for Fig 1E

664   **S3 Dataset.** Individual IEM images of 20 NPCs used for superimposed images of Fig 2B

665   (spFar8-GFP)

666   **S4 Dataset.** Individual IEM images of 20 NPCs used for superimposed images of Fig 3A

667   (spNup211-GFP)

668   **S5 Dataset.** Values of the maximum fluorescence intensity of spNup211-GFP in wild type,

669   *nup131Δ* and *nup132Δ* cells measured for Fig 3C.

670   **S6 Dataset.** Individual IEM images of 20 NPCs used for superimposed images of Fig 4A

671   (pNup120-GFP, spNup85-GFP, spNup96-GFP, spNup37-GFP, spEly5-GFP, spSeh1-GFP,

672   spNup107-GFP and GFP-spNup107)

673   **S7 Dataset.** Values of the distance between spNup85-GFP and mCherry-spNup131 and

674   those between spNup85-GFP and mCherry-spNup132 measured for Fig 4B

675   **S8 Dataset.** Values of the distance between spNup107-GFP and mCherry-spNup131 and

676   those between spNup107-GFP and mCherry-spNup132 measured for Fig 4C

677   **S9 Dataset.** Individual IEM images of 20 NPCs used for superimposed images of Fig 5B

678   (spNup96-spNup107-GFP) and 5C (GFP-spNup132 in the presence of the spNup96-

679   spNup107 fusion protein)

680   **S10 Dataset.** Individual IEM images of 20 NPCs used for superimposed images of Fig

681   6C (full length GFP-spNup131 and GFP-spNup132, and their C-terminal domains in the

682   *nup131Δnup132Δ* mutant cells)

683   **S11 Dataset.** Individual IEM images of 20 NPCs used for superimposed images of Fig

684   7 (inner ring Nups, channel Nups, cytoplasmic ring Nups, transmembrane Nups and

685   nuclear basket Nups)

686

References

687 **References**

688 [1] Rout MP, Aitchison JD, Suprapto A, Hjertaas K, Zhao Y, Chait BT. The yeast

689 nuclear pore complex: composition, architecture, and transport mechanism. J Cell

690 Biol. 2000; 148: 635-651. doi:10.1083/jcb.148.4.635.

691 [2] Cronshaw JM, Krutchinsky AN, Zhang W, Chait BT, Matunis MJ. Proteomic

692 analysis of the mammalian nuclear pore complex. J Cell Biol. 2002; 158: 915-927.

693 doi:10.1083/jcb.200206106.

694 [3] Alber F, Dokudovskaya S, Veenhoff LM, Zhang W, Kipper J, Devos D, et al. The

695 molecular architecture of the nuclear pore complex. Nature. 2007; 450: 695-701.

696 doi:10.1038/nature06405.

697 [4] Bui KH, von Appen A, DiGuilio AL, Ori A, Sparks L, Mackmull MT, et al.

698 Integrated structural analysis of the human nuclear pore complex scaffold. Cell.

699 2013; 155: 1233-1243. doi:10.1016/j.cell.2013.10.055.

700 [5] von Appen A, Kosinski J, Sparks L, Ori A, DiGuilio AL, Vollmer B, et al. *In situ*

701 structural analysis of the human nuclear pore complex. Nature. 2015; 526: 140-

702 143. doi:10.1038/nature15381.

703 [6] Kosinski J, Mosalaganti S, von Appen A, Teimer R, DiGuilio AL, Wan W, et al.

704 Molecular architecture of the inner ring scaffold of the human nuclear pore

705 complex. Science. 2016; 352: 363-365. doi: 10.1126/science.aaf0643.

706 [7] Lin DH, Stuwe T, Schilbach S, Rundlet EJ, Perriches T, Mobbs G, et al.

707 Architecture of the symmetric core of the nuclear pore. Science. 2016; 352:

708 aaf1015. doi:10.1126/science.aaf1015.

709 [8] Onischenko E, Stanton LH, Madrid AS, Kieselbach T, Weis K. Role of the Ndc1

710 interaction network in yeast nuclear pore complex assembly and maintenance. J

711   Cell Biol. 2009; 185:475-491. doi: 10.1083/jcb.200810030.

712   [9]   Eisenhardt N, Redolfi J, Antonin W. Interaction of Nup53 with Ndc1 and Nup155

713   is required for nuclear pore complex assembly. J Cell Sci. 2014; 127: 908-921.

714   doi: 10.1242/jcs.141739.

715   [10]   DeGrasse JA, DuBois KN, Devos D, Siegel TN, Sali A, Field MC, et al. Evidence

716   for a shared nuclear pore complex architecture that is conserved from the last

717   common eukaryotic ancestor. Mol Cell Proteomics. 2009; 8: 2119-2130. doi:

718   10.1074/mcp.M900038-MCP200.

719   [11]   Tamura K, Fukao Y, Iwamoto M, Haraguchi T, Hara-Nishimura I. Identification

720   and characterization of nuclear pore complex components in *Arabidopsis*

721   *thaliana*. Plant Cell. 2010; 22: 4084-4097. doi: 10.1105/tpc.110.079947.

722   [12]   Amlacher S, Sarges P, Flemming D, van Noort V, Kunze R, Devos DP, et al.

723   Insight into structure and assembly of the nuclear pore complex by utilizing the

724   genome of a eukaryotic thermophile. Cell. 2011; 146: 277-286. doi:

725   10.1016/j.cell.2011.06.039.

726   [13]   Obado SO, Brillantes M, Uryu K, Zhang W, Ketaren NE, Chait BT, et al.

727   Interactome mapping reveals the evolutionary history of the nuclear pore

728   complex. PLoS Biol. 2016; 14: e1002365. doi: 10.1371/journal.pbio.1002365.

729   [14]   Knockenhauer KE, Schwartz TU. The nuclear pore complex as a flexible and

730   dynamic gate. Cell. 2016; 164: 1162-1171. doi: 10.1016/j.cell.2016.01.034.

731   [15]   Walther TC, Alves A, Pickersgill H, Loïodice I, Hetzer M, Galy V, et al. The

732   conserved Nup107-160 complex is critical for nuclear pore complex assembly.

733   Cell. 2003; 113: 195-206. doi: 10.1016/S0092-8674(03)00235-6.

734   [16]   Harel A, Orjalo AV, Vincent T, Lachish-Zalait A, Vasu S, Shah S, et al. Removal

735   of a single pore subcomplex results in vertebrate nuclei devoid of nuclear pores.

736   Mol Cell. 2003; 11: 853-864. doi: 10.1016/S1097-2765(03)00116-3.

737   [17] Loïodice I, Alves A, Rabut G, Van Overbeek M, Ellenberg J, Sibarita JB, et al.

738   The entire Nup107-160 complex, including three new members, is targeted as one

739   entity to kinetochores in mitosis. Mol Biol Cell. 2004; 15: 3333-3344.   doi:

740   10.1091/mbc.E03-12-0878.

741   [18] Rasala BA, Orjalo AV, Shen Z, Briggs S, Forbes DJ. ELYS is a dual

742   nucleoporin/kinetochore protein required for nuclear pore assembly and proper

743   cell division. Proc Natl Acad Sci U S A. 2006; 103: 17801-17806. doi:

744   10.1073/pnas.0608484103.

745   [19] Liu HL, De Souza CP, Osmani AH, Osmani SA. The three fungal transmembrane

746   nuclear pore complex proteins of *Aspergillus nidulans* are dispensable in the

747   presence of an intact An-Nup84-120 complex. Mol. Biol. Cell. 2009; 20: 616-630.

748   doi: 10.1091/mbc.E08-06-0628.

749   [20] Thierbach K, von Appen A, Thoms M, Beck M, Flemming D, Hurt E. Protein

750   interfaces of the conserved Nup84 complex from *Chaetomium thermophilum*

751   shown by crosslinking mass spectrometry and electron microscopy. Structure.

752   2013; 21: 1672-1682. doi: 10.1016/j.str.2013.07.004.

753   [21] Kampmann M, Blobel G. Three-dimensional structure and flexibility of a

754   membrane-coating module of the nuclear pore complex. Nat Struct Mol Biol.

755   2009; 16: 782-788. doi: 10.1038/nsmb.1618.

756   [22] Flemming D, Thierbach K, Stelter P, Böttcher B, Hurt E. Precise mapping of

757   subunits in multiprotein complexes by a versatile electron microscopy label. Nat

758   Struct Mol Biol. 2010; 17: 775-778. doi:10.1038/nsmb.1811.

32

759 [23] Fernandez-Martinez J, Phillips J, Sekedat MD, Diaz-Avalos R, Velazquez-Muriel

760   J, Franke JD, et al. Structure-function mapping of a heptameric module in the

761   nuclear pore complex. J. Cell Biol. 2012; 196: 419-434. doi:

762   10.1083/jcb.201109008.

763 [24] Kelley K, Knockenhauer KE, Kabachinski G, Schwartz TU. Atomic structure of

764   the Y complex of the nuclear pore. Nat Struct Mol Biol. 2015; 22: 425-431. doi:

765   10.1038/nsmb.2998.

766 [25] Stuwe T, Correia AR, Lin DH, Paduch M, Lu VT, Kossiakoff AA, et al. Nuclear

767   pores. Architecture of the nuclear pore complex coat. Science. 2015; 347: 1148-

768   1152. doi: 10.1126/science.aaa4136.

769 [26] Kim SJ, Fernandez-Martinez J, Nudelman I, Shi Y, Zhang W, Raveh B, et al.

770   Integrative structure and functional anatomy of a nuclear pore complex. Nature.

771   2018; 555: 475-482. doi: 10.1038/nature26003.

772 [27] Baï SW, Rouquette J, Umeda M, Faigle W, Loew D, Sazer S, et al. The fission

773   yeast Nup107-120 complex functionally interacts with the small GTPase Ran/Spi1

774   and is required for mRNA export, nuclear pore distribution, and proper cell

775   division. Mol Cell Biol. 2004; 24: 6379-6392. doi: 10.1128/MCB.24.14.6379-

776   6392.2004

777 [28] Chen XQ, Du X, Liu J, Balasubramanian MK, Balasundaram D. Identification of

778   genes encoding putative nucleoporins and transport factors in the fission yeast

779   *Schizosaccharomyces pombe*: a deletion analysis. Yeast. 2004; 21: 495-509. doi:

780   10.1002/yea.1115.

781 [29] Asakawa H, Yang HJ, Yamamoto TG, Ohtsuki C, Chikashige Y, Sakata-Sogawa

782   K, et al. Characterization of nuclear pore complex components in fission yeast

33

783   *Schizosaccharomyces pombe*. Nucleus. 2014; 5: 149-162. doi:

784   10.4161/nucl.28487.

785 [30] Yang HJ, Asakawa H, Haraguchi T, Hiraoka Y. Nup132 modulates meiotic spindle

786   attachment in fission yeast by regulating kinetochore assembly. J Cell Biol. 2015;

787   211: 295-308. doi: 10.1083/jcb.201501035.

788 [31] Liu NN, Han TX, Du LL, Zhou JQ. A genome-wide screen for

789   *Schizosaccharomyces pombe* deletion mutants that affect telomere length. Cell

790   Res. 2010; 20: 963-965. doi: 10.1038/cr.2010.107.

791 [32] Nie M, Boddy MN. Pli1(PIAS1) SUMO ligase protected by the nuclear pore-

792   associated SUMO protease Ulp1SENP1/2. J Biol Chem. 2015; 290: 22678-22685.

793   doi: 10.1074/jbc.M115.673038.

794 [33] Whittle JR, Schwartz TU. Architectural nucleoporins Nup157/170 and Nup133

795   are structurally related and descend from a second ancestral element. J Biol Chem.

796   2009; 284: 28442-28452. doi: 10.1074/jbc.M109.023580.

797 [34] Saitoh S, Takahashi K, Yanagida M. Mis6, a fission yeast inner centromere

798   protein, acts during G1/S and forms specialized chromatin required for equal

799   segregation. Cell. 1997; 90: 131-143. doi: 10.1016/S0092-8674(00)80320-7.

800 [35] Matsuda A, Schermelleh L, Hirano Y, Haraguchi T, Hiraoka Y. Accurate and

801   fiducial-marker-free correction for three-dimensional chromatic shift in biological

802   fluorescence microscopy. Sci Rep. 2018; 8:7583. doi: 10.1038/s41598-018-25922-

803   7.

804 [36] Matsuda A. 2018. Chromagnon. Github.

805   https://github.com/macronucleus/chromagnon. 84d4506.

806 [37] Goudreault M, D'Ambrosio LM, Kean MJ, Mullin MJ, Larsen BG, Sanchez A, et

807   al. A PP2A phosphatase high density interaction network identifies a novel

808   striatin-interacting phosphatase and kinase complex linked to the cerebral

809   cavernous malformation 3 (CCM3) protein. Molecular & Cellular Proteomics.

810   2009; 8: 157-171. doi: 10.1074/mcp.M800266-MCP200.

811 [38] Frost A, Elgort MG, Brandman O, Ives C, Collins SR, Miller-Vedam L, et al.

812   Functional repurposing revealed by comparing *S. pombe* and *S. cerevisiae* genetic

813   interactions. Cell. 2012; 149: 1339-1352. doi: 10.1016/j.cell.2012.04.028.

814 [39] Singh NS, Shao N, McLean JR, Sevugan M, Ren L, Chew TG, et al. SIN-

815   inhibitory phosphatase complex promotes Cdc11p dephosphorylation and

816   propagates SIN asymmetry in fission yeast. Curr Biol. 2011; 21: 1968-1978. doi:

817   10.1016/j.cub.2011.10.051.

818 [40] Bae JA, Moon D, Yoon JH. Nup211, the fission yeast homolog of Mlp1/Tpr, is

819   involved in mRNA export. J Microbiol. 2009; 47:337-343. doi: 10.1007/s12275-

820   009-0125-7.

821 [41] Strambio-de-Castillia C, Blobel G, Rout MP. Proteins connecting the nuclear pore

822   complex with the nuclear interior. J Cell Biol. 1999; 144: 839-855. doi:

823   10.1083/jcb.144.5.839.

824 [42] Krull S, Thyberg J, Björkroth B, Rackwitz HR, Cordes VC. Nucleoporins as

825   components of the nuclear pore complex core structure and Tpr as the

826   architectural element of the nuclear basket. Mol Biol Cell. 2004; 15: 4261-4277.

827   doi: 10.1091/mbc.e04-03-0165.

828 [43] Asakawa H, Mori C, Ohtsuki C, Iwamoto M, Hiraoka Y, Haraguchi T.

829   Uncleavable Nup98-Nup96 is functional in the fission yeast *Schizosaccharomyces*

830   *pombe*. FEBS Open Bio. 2015; 5: 508-514. doi: 10.1016/j.fob.2015.06.004.

831   [44] Berke IC, Boehmer T, Blobel G, Schwartz TU. Structural and functional analysis

832   of Nup133 domains reveals modular building blocks of the nuclear pore complex.

833   J Cell Biol. 2004; 167: 591-597. doi: 10.1083/jcb.200408109.

834   [45] Iwamoto M, Asakawa H, Ohtsuki C, Osakada H, Koujin T, Hiraoka Y, et al.

835   Monoclonal antibodies recognize Gly-Leu-Phe-Gly repeat of nucleoporin Nup98

836   of *Tetrahymena*, yeasts, and humans. Monoclon Antib Immunodiagn Immunother.

837   2013; 32: 81-90. doi: 10.1089/mab.2012.0118.

838   [46] Hodel AE, Hodel MR, Griffis ER, Hennig KA, Ratner GA, Xu S, et al. The three-

839   dimensional structure of the autoproteolytic, nuclear pore-targeting domain of the

840   human nucleoporin Nup98. Mol Cell. 2002; 10: 347-358. doi: 10.1016/S1097-

841   2765(02)00589-0.

842   [47] Griffis ER, Xu S, Powers MA. Nup98 localizes to both nuclear and cytoplasmic

843   sides of the nuclear pore and binds to two distinct nucleoporin subcomplexes. Mol

844   Biol Cell. 2003; 14: 600-610. doi: 10.1091/mbc.E02-09-0582.

845   [48] Ratner GA, Hodel AE, Powers MA. Molecular determinants of binding between

846   Gly-Leu-Phe-Gly nucleoporins and the nuclear pore complex. J Biol Chem. 2007;

847   282: 33968-33976. doi: 10.1074/jbc.M707911200.

848   [49] Stuwe T, von Borzyskowski LS, Davenport AM, Hoelz A. Molecular basis for the

849   anchoring of proto-oncoprotein Nup98 to the cytoplasmic face of the nuclear pore

850   complex. J Mol Biol. 2012; 419: 330-346. doi: 10.1016/j.jmb.2012.03.024.

851   [50] Salas-Pino S, Gallardo P, Barrales RR, Braun S, Daga RR. The fission yeast

852   nucleoporin Alm1 is required for proteasomal degradation of kinetochore

853   components. J Cell Biol. 2017; 216:3591-3608. doi: 10.1083/jcb.201612194.

854   [51] Maimon T, Elad N, Dahan I, Medalia O. The human nuclear pore complex as

855   revealed by cryo-electron tomography. Structure. 2012; 20: 998-1006. doi:

856   10.1016/j.str.2012.03.025.

857   [52] D'Angelo MA, Anderson DJ, Richard E, Hetzer MW. Nuclear pores form de novo

858   from both sides of the nuclear envelope. Science. 2006; 312: 440-443. doi:

859   10.1126/science.1124196.

860   [53] Lutzmann M, Kunze R, Buerer A, Aebi U, Hurt E. Modular self-assembly of a Y-

861   shaped multiprotein complex from seven nucleoporins. EMBO J. 2002; 21: 387-

862   397. doi: 10.1093/emboj/21.3.387.

863   [54] Ori A, Banterle N, Iskar M, Andrés-Pons A, Escher C, Bui KH, et al. Cell type-

864   specific nuclear pores: a case in point for context-dependent stoichiometry of

865   molecular machines. Mol Syst Biol. 2013; 9: 648. doi: 10.1038/msb.2013.4.

866   [55] Belgareh N, Rabut G, Baï SW, van Overbeek M, Beaudouin J, Daigle N, et al. An

867   evolutionarily conserved NPC subcomplex, which redistributes in part to

868   kinetochores in mammalian cells. J Cell Biol. 2001; 154: 1147-1160. doi:

869   10.1083/jcb.200101081.

870   [56] Orjalo AV, Arnaoutov A, Shen Z, Boyarchuk Y, Zeitlin SG, Fontoura B, et al. The

871   Nup107-160 nucleoporin complex is required for correct bipolar spindle

872   assembly. Mol Biol Cell. 2006; 17: 3806-3818. doi: 10.1091/mbc.E05-11-1061.

873   [57] Zuccolo M, Alves A, Galy V, Bolhy S, Formstecher E, Racine V, et al. The human

874   Nup107-160 nuclear pore subcomplex contributes to proper kinetochore

875   functions. EMBO J. 2007; 26: 1853-1864. doi: 10.1038/sj.emboj.7601642.

876   [58] Platani M, Santarella-Mellwig R, Posch M, Walczak R, Swedlow JR, Mattaj IW.

877   The Nup107-160 nucleoporin complex promotes mitotic events via control of the

878   localization state of the chromosome passenger complex. Mol Biol Cell. 2009; 20:

37

879   5260-5275. doi: 10.1091/mbc.E09-05-0377.

880 [59] Mishra RK, Chakraborty P, Arnaoutov A, Fontoura BM, Dasso M. The Nup107-

881   160 complex and gamma-TuRC regulate microtubule polymerization at

882   kinetochores. Nat Cell Biol. 2010; 12: 164-169. doi: 10.1038/ncb2016.

883 [60] Moreno CS, Lane WS, Pallas DC. A mammalian homolog of yeast MOB1 is both

884   a member and a putative substrate of striatin family-protein phosphatase 2A

885   complexes. J. Biol. Chem. 2001; 276: 24253–24260. doi:

886   10.1074/jbc.M102398200.

887 [61] Iwamoto M, Osakada H, Mori C, Fukuda Y, Nagao K, Obuse C,et al.

888   Compositionally distinct nuclear pore complexes of functionally distinct

889   dimorphic nuclei in the ciliate *Tetrahymena*. J Cell Sci. 2017; 130: 1822-1834.

890   doi: 10.1242/jcs.199398.

891 [62] Mosalaganti S, Kosinski J, Albert S, Schaffer M, Strenkert D, Salomé PA, et al. In

892   situ architecture of the algal nuclear pore complex. Nature Comm. 2018; 9: 236.

893   doi : 10.1038/s41467-018-04739-y.

894 [63] Karrer KM. Nuclear dualism. Methods Cell Biol. 2012; 109: 29-52.   doi:

895   10.1016/B978-0-12-385967-9.00003-7.

896 [64] Cho AR, Yang KJ, Bae Y, Bahk YY, Kim E, Lee H, et al. Tissue-specific

897   expression and subcellular localization of ALADIN, the absence of which causes

898   human triple A syndrome. Exp. Mol. Med. 2009; 41: 381–386. doi:

899   10.3858/emm.2009.41.6.043.

900 [65] Olsson M, Schéele S, Ekblom P. Limited expression of nuclear pore membrane

901   glycoprotein 210 in cell lines and tissues suggests cell-type specific nuclear pores

902   in metazoans. Exp Cell Res. 2004; 292, 359-370. doi:

903   10.1016/j.yexcr.2003.09.014.

904   [66] D'Angelo MA, Raices M, Panowski SH, Hetzer MW. Age-dependent

905   deterioration of nuclear pore complexes causes a loss of nuclear integrity in

906   postmitotic cells. Cell. 2009; 136: 284-295. doi:10.1016/j.cell.2008.11.037.

907   [67] D'Angelo MA, Gomez-Cavazos JS, Mei A, Lackner DH, Hetzer MW. A change in

908   nuclear pore complex composition regulates cell differentiation. Dev Cell. 2012;

909   22: 446-458. doi: 10.1016/j.devcel.2011.11.021.

910   [68] Raices M, D'Angelo MA. Nuclear pore complex composition: a new regulator of

911   tissue-specific and developmental functions. Nat Rev Mol Cell Biol. 2012; 13:

912   687-699. doi: 10.1038/nrm3461.

913   [69] Moreno S, Klar A, Nurse P. Molecular genetic analysis of fission yeast

914   *Schizosaccharomyces pombe*. Methods Enzymol. 1991; 194: 795-823. doi:

915   10.1016/0076-6879(91)94059-L.

916   [70] Bähler J, Wu JQ, Longtine MS, Shah NG, McKenzie A 3rd, Steever AB, et al.

917   Heterologous modules for efficient and versatile PCR-based gene targeting in

918   *Schizosaccharomyces pombe*. Yeast. 1998; 14: 943-951. doi: 10.1002/(SICI)1097-

919   0061(199807)14:10<943::AID-YEA292>3.0.CO;2-Y.

920   [71] Chikashige Y, Kurokawa R, Haraguchi T, Hiraoka Y. Meiosis induced by

921   inactivation of Pat1 kinase proceeds with aberrant nuclear positioning of

922   centromeres in the fission yeast *Schizosaccharomyces pomb*e. Genes Cells. 2004;

923   9: 671-684. doi: 10.1111/j.1356-9597.2004.00760.x.

924   [72] Boulanger J, Kervrann C, Bouthemy P. A simulation and estimation framework

925   for intracellular dynamics and trafficking in video-microscopy and fluorescence

926   imagery. Med. Image Anal. 2009; 13: 132–142. doi: 10.1016/j.media.2008.06.017.

927 [73] Sawin KE, Nurse P. Photoactivation of green fluorescent protein. Curr Biol. 1997;

928   7: R606-607. doi: 10.1016/S0960-9822(06)00313-7

929 [74] Matsuda A, Shao L, Boulanger J, Kervrann C, Carlton PM, Kner P, et al.

930   Condensed mitotic chromosome structure at nanometer resolution using PALM

931   and EGFP- histones. PLoS ONE. 2010; 5: e12768. doi:

932   10.1371/journal.pone.0012768.

933 [75] Hakhverdyan Z, Domanski M, Hough LE, Oroskar AA, Oroskar AR, Keegan S, et

934   al. Rapid, optimized interactomic screening. Nat Methods. 2015; 12: 553-560. doi:

935   10.1038/nmeth.3395.

936 [76] Obado SO, Field MC, Chait BT, Rout MP. High-efficiency isolation of nuclear

937   envelope protein complexes from Trypanosomes. Methods Mol Biol. 2016; 1411:

938   67-80. doi: 10.1007/978-1-4939-3530-7_3.

939 [77] Nozawa RS, Nagao K, Igami KT, Shibata S, Shirai N, Nozaki N, et al. Human

940   inactive X chromosome is compacted through a polycomb-independent

941   SMCHD1-HBiX1 pathway. Nature Struct Mol Biol. 2013; 20: 566–573. doi:

942   10.1038/nsmb.2532.

943

944

945

946   **Figure legends**

947

948   **Fig 1. Localization of spNup131 and spNup132 at the NPC.**

949   **(A)** IEM of GFP-spNup131 and GFP-spNup132. Arrows indicate the nuclear pores.

950   Scale bar, 100 nm. **(B)** Quantitative representation of IEM for N-terminally tagged

951   spNup131 and spNup132. (left) A montage image of 20 immunoelectron micrographs.

952   The diameter of the circle is 200 nm. (right) A schematic drawing illustrating the

953   distribution of immunogold particles shown in the montage image. Red dots represent

954   the pore centers. **(C)** Quantitative representation of IEM for C-terminally tagged

955   spNup131 and spNup132. Montage pictures and distributions of immunogold particles

956   are shown as described in **(B)**. IEM micrographs used for the quantitative analysis are

957   available in S1 Dataset. **(D)** Fluorescence microscopy of a nucleus simultaneously

958   expressing spNup131 and spNup132 fused to GFP and mCherry in living cells. (left) A

959   nucleus expressing GFP-spNup131 and mCherry-spNup132. Green, GFP-spNup131;

960   Magenta, mCherry-spNup132. (right) A nucleus expressing mCherry-spNup131 and

961   GFP-spNup132. Magenta, mCherry-spNup132; Green, GFP-spNup131. Scale bar, 1

962   μm. **(E)** Distances between spNup131 and spNup132 in living cells. Results from cells

963   expressing GFP-spNup131 and mCherry-spNup132 (n=90, left) and results from cells

964   expressing mCherry-spNup131 and GFP-spNup132 (n=138, right) are shown in the box

965   plot: values of the distance determined in individual cells are shown in S2 Dataset.

966   Center lines show the medians; box limits indicate the 25th and 75th percentiles.

967   Whiskers extend to the 5th and 95th percentiles. The diagram on the right shows the

968   positions of spNup131 and spNup132 within the NPC.

969

41

970 **Fig 2. spNup131 is required for spFar8 localization on the cytoplasmic side of the**

971 **NPC.**

972 **(A)** Localization of spFar8-GFP in wild type, *nup131Δ,* and *nup132Δ* cells. spFar8-GFP

973 was expressed in the indicated strains, and cells exponentially growing in EMM2 liquid

974 medium were observed by FM. spCut11-mCherry was observed as an NPC marker.

975 Scale bar, 10 μm. **(B)** IEM of spFar8-GFP. For quantitative representation, a montage

976 image of 20 immunoelectron micrographs and a schematic drawing illustrating the

977 distribution of immunogold particles are shown. The red point indicates the pore center.

978 IEM micrographs used for the quantitative analysis are available in S3 Dataset. **(C)**

979 Western blot analysis of spFar8-GFP. Whole cell extracts were prepared from wild type,

980 *nup131Δ,* and *nup132Δ* cells expressing spFar8-GFP and subjected to SDS-PAGE and

981 Western blot analysis. spFar8-GFP was detected with anti-GFP antibody. spNup98 was

982 detected with anti-Nup98 antibody (13C2) as a loading control. The arrow indicates the

983 position of spFar8-GFP. Small dots on the left indicate positions of molecular weight

984 markers. **(D)** Overexpression of spNup131 and spNup132 in *nup131Δ* cells expressing

985 spFar8-GFP. spNup131 or spNup132 were overexpressed in *nup131Δ* cells and

986 localization of spFar8-GFP and spCut11-mCherry was observed by FM. Empty vector

987 was also introduced for a control strain. Scale bar, 10μm. **(E)** Quantitative analysis of

988 cells exhibiting spFar8-GFP at the NE in the experiment described in **(D)**. Cells

989 observed were: 81, 102, and 130 for vector, spNup131[op], and spNup132[op], respectively.

990

991 **Fig 3. spNup132 is required for the distribution of the nucleoplasmic nucleoporin**

992 **spNup211 at the NPC.**

993 **(A)** IEM of spNup211-GFP. For quantitative representation, a schematic drawing

42

994   illustrating the distribution of immunogold particles based on 20 immunoelectron

995   micrographs is shown. The red point indicates the pore center. IEM micrographs used

996   for the quantitative analysis are available in S4 Dataset. **(B)** FM of spNup211-GFP in

997   living cells. Arrows indicate bright dots observed in *nup132Δ* cells. Scale bar, 10 μm.

998   **(C)** Maximum intensity values of spNup211-GFP and spCut11-mCherry in wild-type

999   (n=76), *nup131Δ* (n=50), and *nup132Δ* (n=73) cells: values of the maximum intensity

1000   determined in individual cells are shown in S5 Dataset. In the box plot, the center lines

1001   show the medians; box limits indicate the 25th and 75th percentiles. Whiskers extend to

1002   the 5th and 95th percentiles. Averages (±standard deviations) are 110.1±22.7,

1003   105.0±21.5 and 154.7±64.1 for spNup211-GFP, and 18.0±3.2, 17.6±3.0 and 18.8±4.0

1004   for spCut11-mCherry in wild-type, *nup131Δ*, and *nup132Δ*, respectively. *p* values

1005   shown at the bottom are calculated by the Mann-Whitney's U-test.

1006

1007   **Fig 4. Localization of Nup107-160 subcomplex orthologs.**

1008   **(A)** IEM of *S. pombe* Nup107-160 subcomplex orthologs. Immunogold distributions of

1009   the projected immunoelectron micrographs are shown as a quantitative representation.

1010   To confirm the accessibility of the nucleus to immunogold particles, spMis6-GFP was

1011   used. spMis6-positive nuclei were evaluated for staining with anti-GFP antibody. IEM

1012   micrographs used for the quantitative analysis are available in S6 Dataset. **(B)** Position

1013   of spNup85-GFP determined by high-precision distance measurements using FM.

1014   **(upper panel)** FM images of a nucleus expressing spNup85-GFP and mCherry-

1015   spNup131 or mCherry–spNup132. Green, spNup85-GFP; magenta, mCherry-spNup131

1016   or mCherry-spNup132. Scale bar, 1 μm. **(lower panel)** Distance between spNup85-GFP

1017   and mCherry-spNup131 (left) or mCherry-spNup132 (right). The relative positions of

43

1018 spNup131 and spNup132 to spNup85 are shown in the box plot: center lines show the

1019 medians; box limits indicate the 25th and 75th percentiles; whiskers extend to the 5th

1020 and 95th percentiles. n, cell number examined. Values of the distance determined in

1021 individual cells are shown in S7 Dataset. The diagram on the right shows the positions

1022 of spNup85, spNup131 and spNup132 within the NPC. **(C)** Position of spNup107-GFP

1023 determined by high-precision distance measurements using FM. **(upper panel)** FM

1024 images of a nucleus expressing spNup107-GFP and mCherry-spNup131 or mCherry–

1025 spNup132. Green, spNup107-GFP; magenta, mCherry-spNup131 or mCherry-

1026 spNup132. Scale bar, 1 μm. **(lower panel)** Distance between spNup107-GFP and

1027 mCherry-spNup131 (left) or mCherry-spNup132 (right). The relative positions of

1028 spNup131 and spNup132 to spNup107 are shown in the box plot as described in **(B)**.

1029 Values of the distance determined in individual cells are shown in S8 Dataset. The

1030 diagram on the right shows the positions of spNup107, spNup131 and spNup132 within

1031 the NPC. **(D)** A schematic drawing showing the localization of Nup107-160

1032 subcomplex orthologs in *S. pombe*.

1033

1034 **Fig 5. Localization and functional analysis of an spNup96-spNup107 fusion Nup.**

1035 **(A)** Western blot analysis of the spNup96-spNup107-GFP fusion protein. Asterisks

1036 represent non-specific cross reactions of the anti-GFP antibody. **(B)** IEM of the

1037 spNup96-spNup107 fusion protein. Immunogold distribution of the projected

1038 immunoelectron micrographs is shown. IEM micrographs used for the quantitative

1039 analysis are available in S9 Dataset. **(C)** IEM of GFP-spNup132 in wild type and

1040 spNup96-spNup107 fusion backgrounds. Localization of GFP-spNup132 in a wild type

1041 background is taken from the data shown in **Fig 1B**. IEM micrographs used for the

44

1042 quantitative analysis are available in S9 Dataset. **(D)** A cell growth assay in the presence

1043 (+TBZ) or absence (-TBZ) of TBZ. Five-fold serial dilutions of wild type and spNup96-

1044 spNup107 fusion strains were spotted on YES medium containing or lacking TBZ and

1045 incubated for 3 days. **(E)** Time-lapse observation of *S. pombe* cells (wt or spNup96-

1046 spNup107 fusion strains) undergoing meiosis. Cells expressing mCherry-fused α-

1047 tubulin (spAtb2) were induced to enter meiosis. The duration of meiosis I and II was

1048 determined as the time the spindle was present. Dotted lines show cell shapes. The time

1049 0 indicates the time of the first appearance of meiosis I spindle formation.

1050 Representative images are shown (number of cells observed: 32 for wild type and 33 for

1051 spNup96-spNup107). **(F)** Statistical analysis for images obtained in **(E)**. Duration of

1052 meiosis I and II. Error bars represent standard deviations. The duration of meiosis I was

1053 28.4 ± 3.0 min in wild type and 37.9 ± 6.3 min in spNup96-spNup107 fusion cells. The

1054 duration of meiosis II was 25.8 ± 1.8 min in wild type and 29.8 ± 2.9 min in spNup96-

1055 spNup107 fusion cells. Asterisks indicate statistical significance ($p < 0.0001$) between

1056 the indicated strains by Welch's t-test. Number of cells observed: 32 for wild type and

1057 33 for spNup96-spNup107. **(G)** Abnormal spore formation was observed in the

1058 spNup96-spNup107 fusion background. More than 200 asci were counted for each

1059 strain.

1060

1061 **Fig 6. Localization of the spNup131 and spNup132 domains.**

1062 **(A)** Schematics of the spNup131 and spNup132 fragments. Magenta represents peptides

1063 from spNup131 and light blue represents peptides from spNup132. **(B)** Localization of

1064 spNup131 and spNup132 fragments as determined by FM. GFP-fused fragments were

1065 expressed under the spNup132 promoter in the background of the *nup131Δ nup132Δ*

45

1066   double mutant. spCut11-mCherry served as an NPC marker. Scale bar, 5 μm. **(C)** IEM

1067   of the spNup131 and spNup132 fragments. Projection images (left) and immunogold

1068   distributions (right) are shown as described in the legend of **Fig 1B**. The red points

1069   indicate the pore centers. IEM micrographs used for the quantitative analysis are
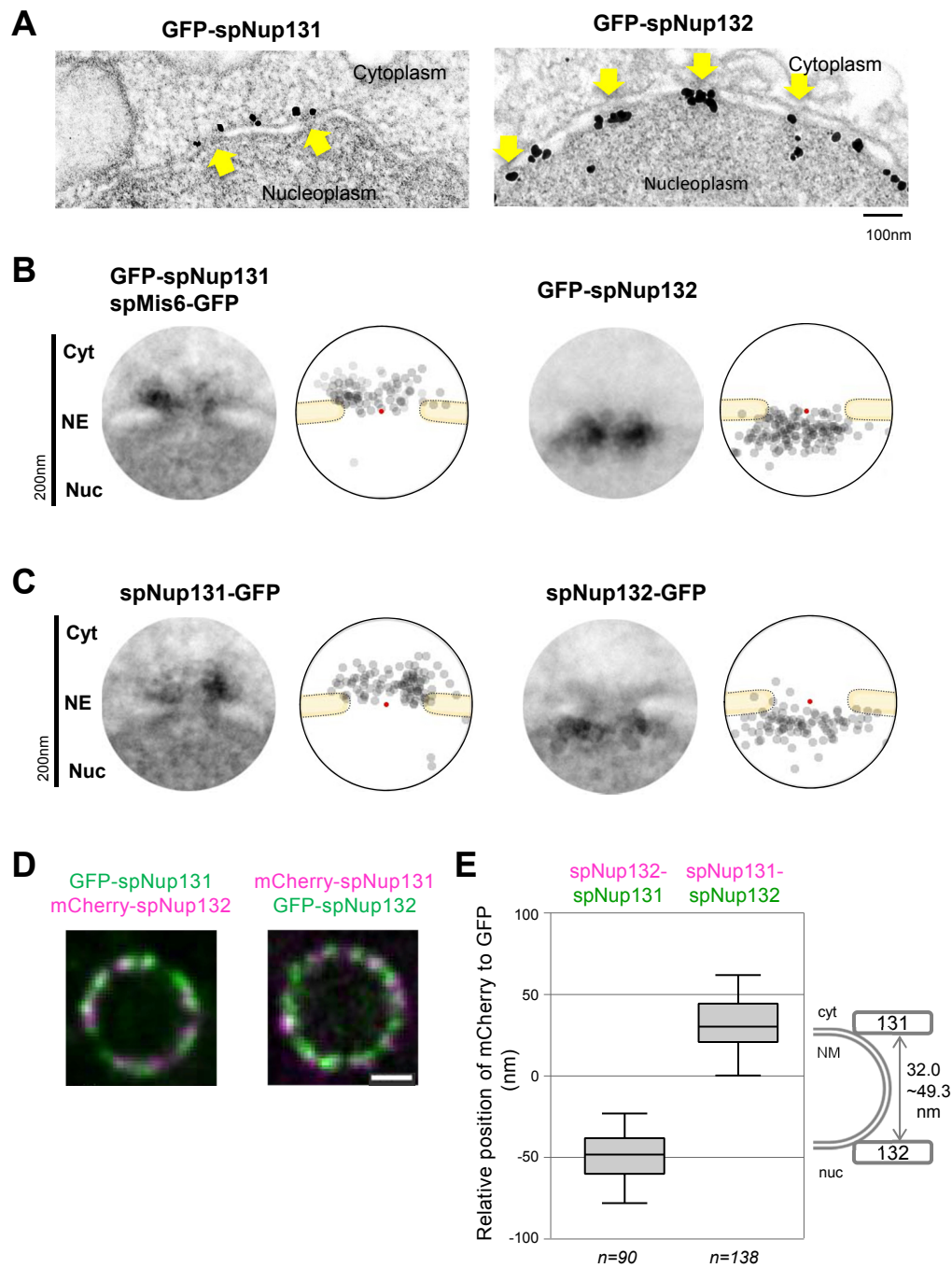
1070   available in S10 Dataset.

1071

1072   **Fig 7. IEM of *S. pombe* nucleoporins.**

1073   **(A)** Inner ring Nups. **(B)** Channel Nups. IEM for spNup98 was performed using an anti-

1074   Nup98 antibody (13C2) for the wild type strain and an anti-GFP antibody for the

1075   spNup98-GFP strain. **(C)** Cytoplasmic ring Nups. **(D)** Transmembrane Nups. **(E)**

1076   Nuclear basket Nups. The localization of the other nuclear basket Nup, spNup211, is

1077   shown in **Fig 3A**. Immunogold distributions are shown based on the projected

1078   immunoelectron micrographs for quantitative representation. The red points indicate the

1079   pore centers. IEM micrographs used for the quantitative analysis are available in S11

1080   Dataset.

1081

1082   **Fig 8. Model of the *S. pombe* NPC.**

1083   The positions of the *S. pombe* Nups and the relative numbers of the Nup107-160

1084   subcomplex Nups making up a single unit of the 8-fold rotational symmetrical structure

1085   of the *S. pombe* NPC are shown. The positions of the subcomplexes were deduced based

1086   on the IEM analysis in this study. The numbers of the Nup107-160 subcomplex

1087   components were deduced based on the FM and biochemical analysis reported

1088   previously [29]: spNup131 (1 molecule, dark blue), the spNup120-spNup85-spNup96-

1089   spNup37-spEly5 complex (2 molecules each, dark green), spSeh1 (1 molecule, light

46

1090   green), spNup107 (1 molecule, orange), spNup132 (6 molecules, right blue).
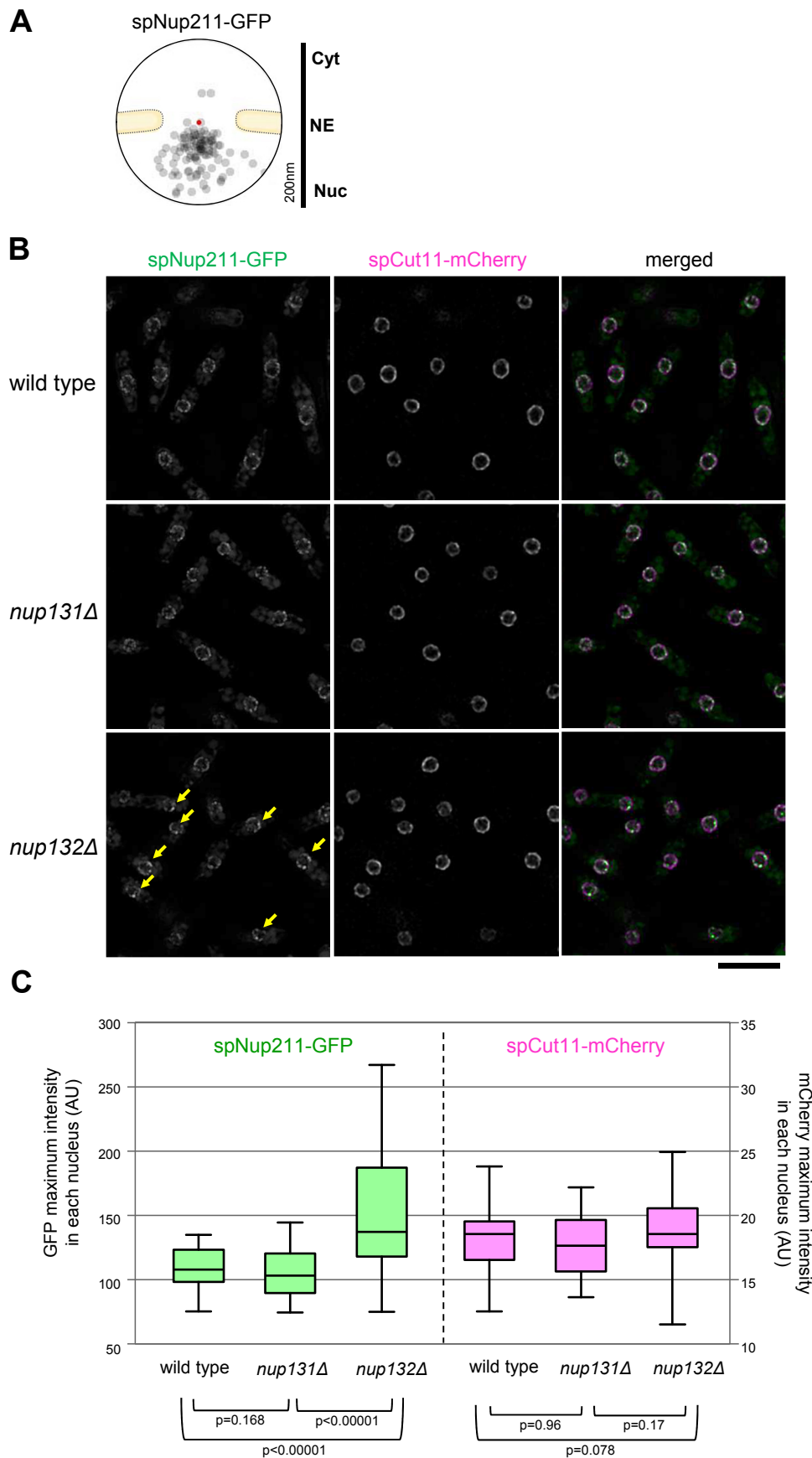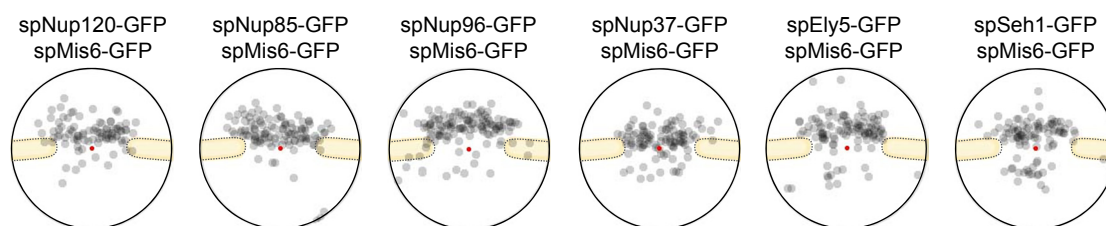
1091

Asakawa et al. Fig 1
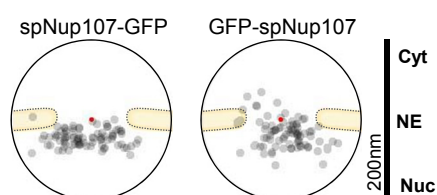
Asakawa et al. Fig 2
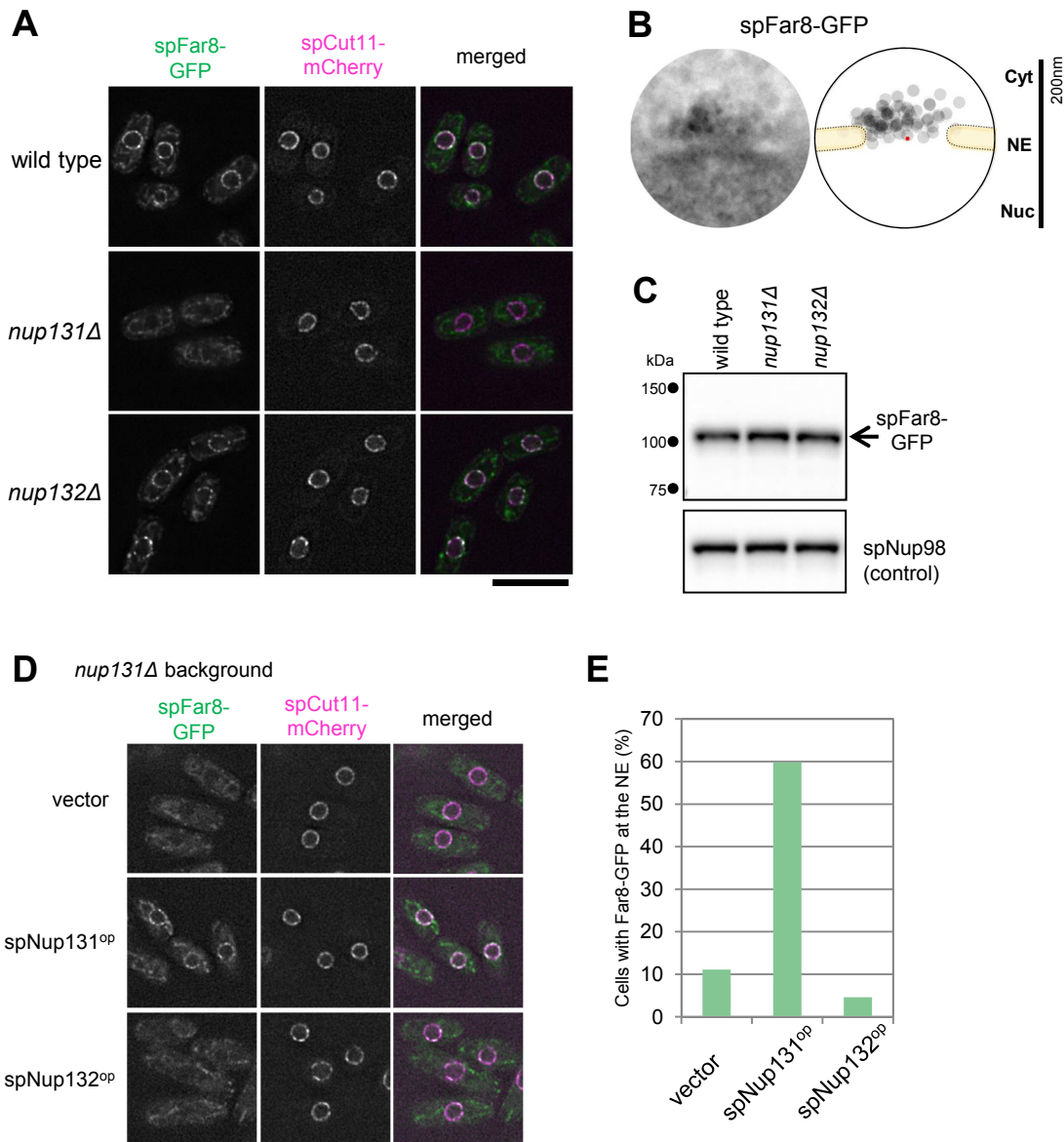
Asakawa et al. Fig 3

A

spNup211-GFP

B

| spNup211-GFP | spCut11-mCherry | merged |

wild type

nup131Δ

nup132Δ

C

Asakawa et al. Fig 4
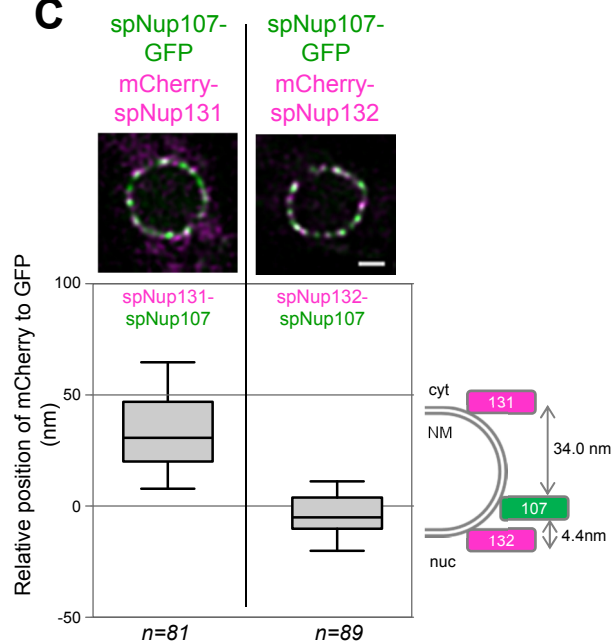
Asakawa et al. Fig 5

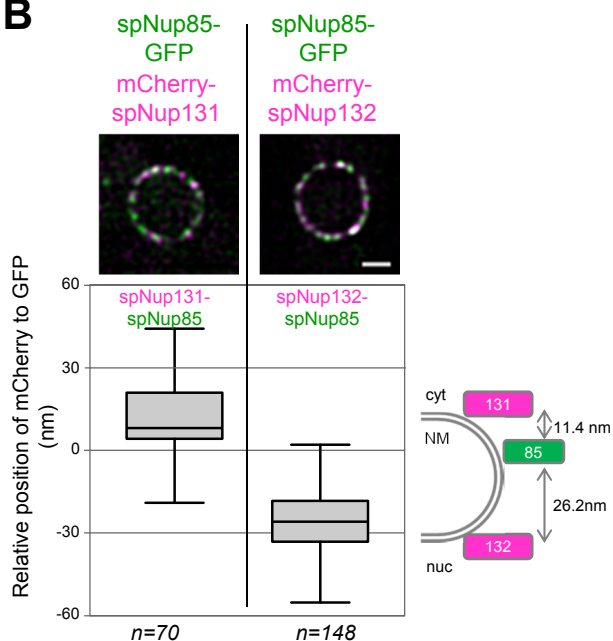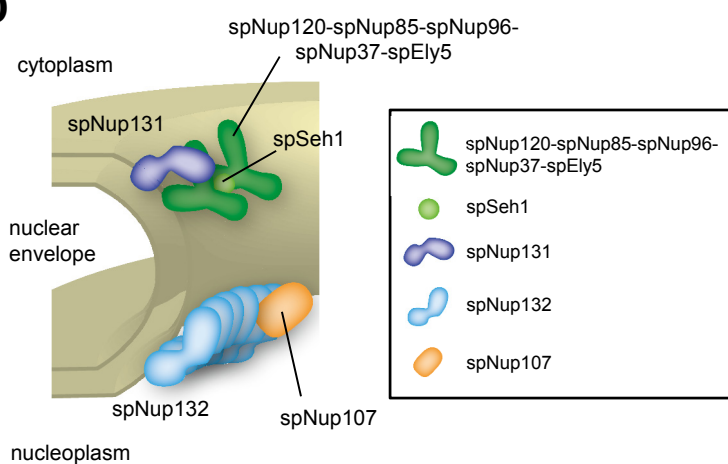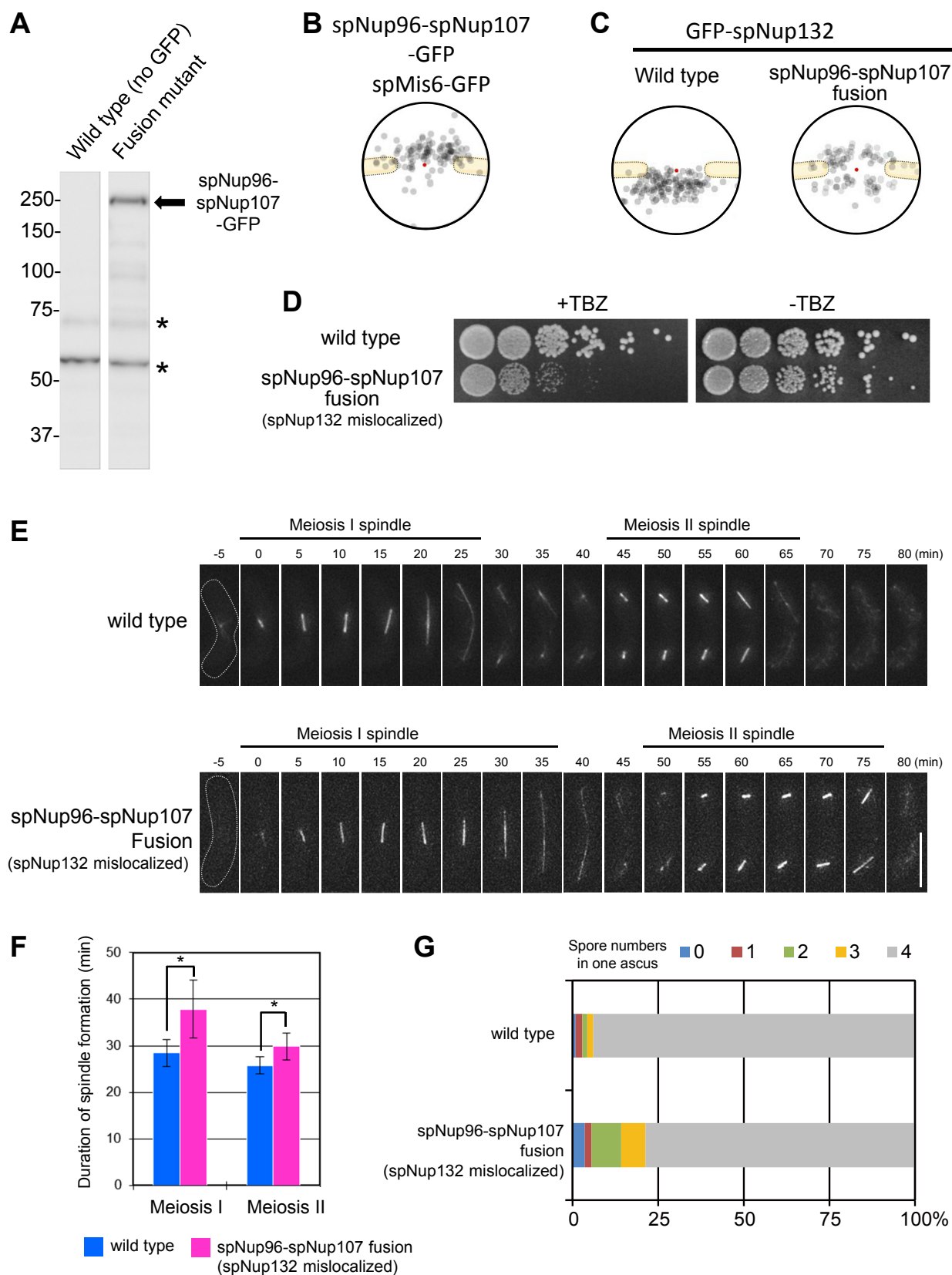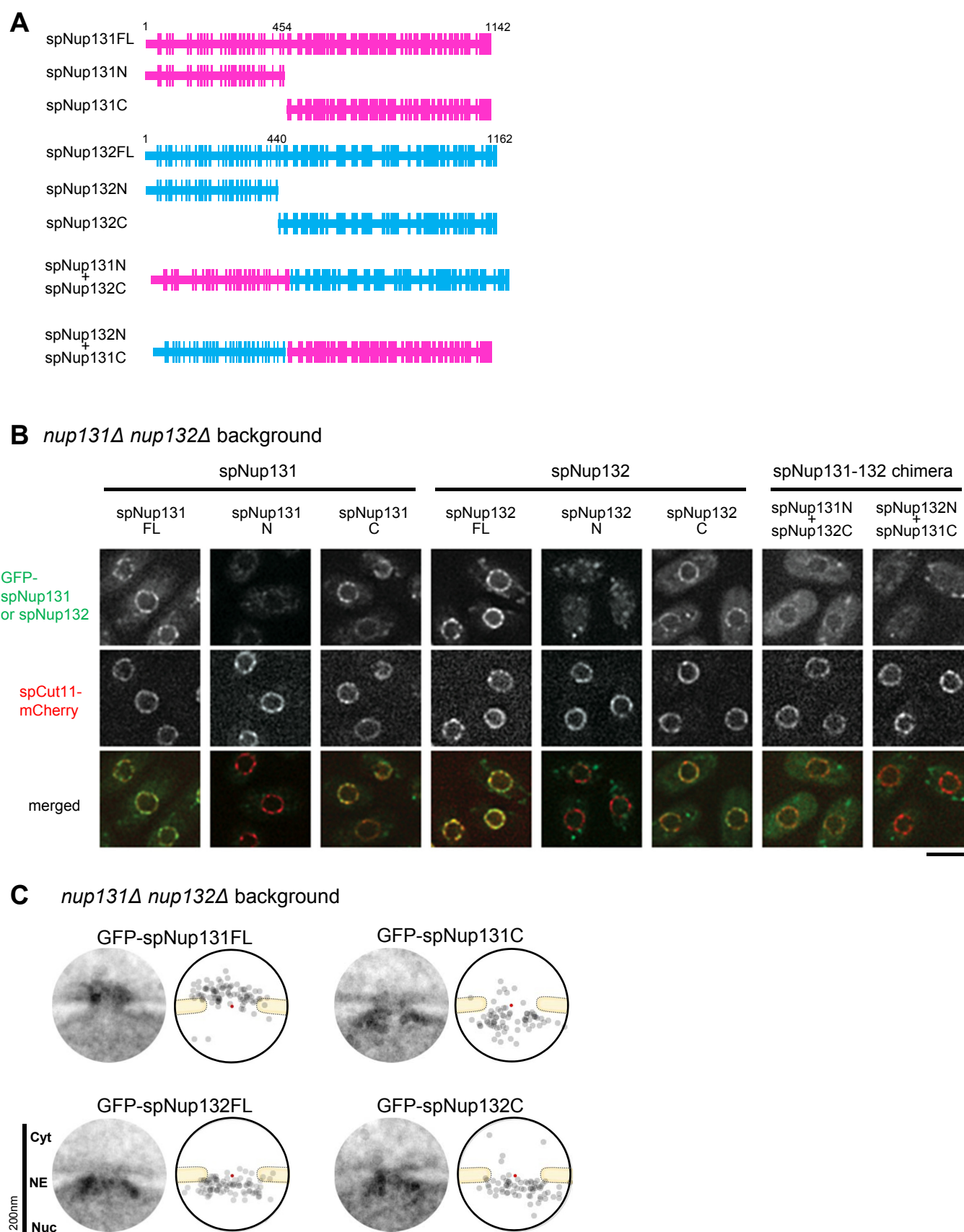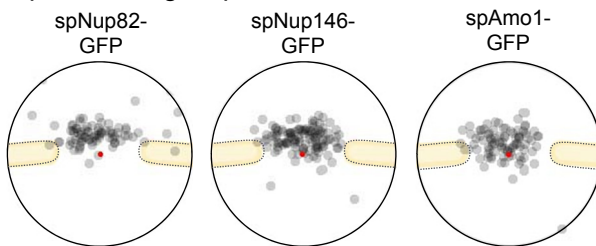# Asakawa et al. Fig 6
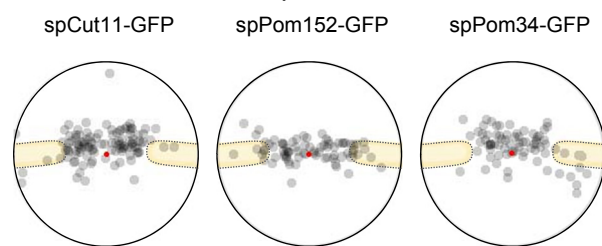
Asakawa et al. Fig 7

A Inner ring Nups

GFP-spNup97 GFP-spNpp106 GFP-spNup184 GFP-spNup186 GFP-spNup40 spNup155-GFP

B Channel Nups

spNup44-GFP spNup45-GFP spNup98-GFP spNup98 (anti-Nup98) GFP-spNsp1

C Cytoplasmic ring Nups

spNup82-GFP spNup146-GFP spAmo1-GFP

D Transmembrane Nups

spCut11-GFP spPom152-GFP spPom34-GFP

E Nuclear basket Nups

spNup60-GFP GFP-spNup61 GFP-spNup124 spAlm1-GFP

Cyt

NE

Nuc

200nm

Asakawa et al. Fig 8